

Department of Physics and Astronomy  
University of Heidelberg

Master thesis

in Physics

submitted by

Alessandro Rizzi

born in Cittiglio (VA), Italy

2023

Spectral eigenfunction decomposition  
of a Fokker-Planck operator  
for relativistic heavy-ion collisions

This Master thesis has been carried out by Alessandro Rizzi

at the

Institute of Theoretical Physics

under the supervision of

Herrn Prof. Georg Wolschin

and

Herrn Prof. Andreas Mielke

Institute of Theoretical Physics

## **Zusammenfassung**

Ziel dieser Arbeit ist es, eine spektrale Lösungsmethode anzuwenden, um die Genauigkeit eines zuvor entwickelten nichtgleichgewichts-statistischen Modells zur Beschreibung der Thermalisierung geladener Hadronen in relativistischen Schwerionenkollisionen zu verbessern. Die Trajektorien im Phasenraum der Teilchen werden als ein stochastischer Drift-Diffusionsprozess behandelt, der zu einer Fokker-Planck-Gleichung (FPE) für die Ein-Teilchen-Wahrscheinlichkeitsverteilung führt. Die Drift- und Diffusionskoeffizienten werden aus dem erwarteten asymptotischen Zustand durch geeignete Fluktuations-Dissipations-Beziehungen abgeleitet, und die resultierende FPE mit nichtlinearen Koeffizientenfunktionen wird anschließend numerisch auf der Basis einer Entwicklung nach Eigenfunktionen gelöst. Die erhaltene zeitabhängige Teilchenverteilung wird dann mit experimentellen Daten des Large Hadron Colliders verglichen, um die freien Parameter des Modells anzupassen.

## **Abstract**

A spectral solution method is implemented to improve the accuracy of a previously developed non-equilibrium statistical model describing produced charged hadron thermalization in relativistic heavy-ion collisions. The particle's phase-space trajectories are treated as a drift-diffusion stochastic process, leading to a Fokker-Planck equation (FPE) for the single-particle probability distribution function. The drift and diffusion coefficients are derived from the expected asymptotic state via appropriate fluctuation-dissipation relations, and the resulting FPE with non-linear coefficient functions is then numerically solved with a spectral eigenfunction decomposition. The resulting time-dependent particle distribution is then compared to experimental data from the Large Hadron Collider to tune the free parameters of the model.



# Contents

<b>1</b>	<b>Introduction</b>	<b>1</b>
<b>2</b>	<b>Probability theory and stochastic processes</b>	<b>5</b>
2.1	Basis of probability theory . . . . .	5
2.2	Random variables and probability distributions . . . . .	6
2.2.1	Probability mass and density functions . . . . .	7
2.2.2	Independence, joint and conditional probability . . . . .	9
2.3	Stochastic processes . . . . .	10
2.3.1	Markov processes . . . . .	11
2.3.2	The Random walk and the Wiener process . . . . .	12
2.3.3	Diffusion processes . . . . .	13
2.4	The Fokker-Planck equation . . . . .	14
2.4.1	The Kramers-Moyal expansion . . . . .	14
2.4.2	The Fokker-Planck equation in diffusion processes . . . . .	15
2.4.3	Detailed balance and fluctuation-dissipation relations . . . . .	16
2.4.4	Eigenfunction expansion . . . . .	17
2.4.5	The Ornstein-Uhlenbeck process . . . . .	19
<b>3</b>	<b>Relativistic heavy-ion collisions as a diffusion process</b>	<b>21</b>
3.1	Relativistic diffusion . . . . .	21
3.2	System and observables . . . . .	22
3.3	Drift-diffusion model . . . . .	25
3.3.1	Dimensionless formulation . . . . .	26
3.3.2	Multiple-sources ansatz . . . . .	26
3.4	Charged-hadron thermalization . . . . .	27
3.4.1	Initial state . . . . .	27
3.4.2	Asymptotic state . . . . .	30
3.5	Spectral method of solution . . . . .	33
3.5.1	Spectral representation of the 1- $d$ FPO . . . . .	33
3.5.2	Representation of the 2- $d$ Schrödinger operator . . . . .	35

## *Contents*

<b>4</b>	<b>Results</b>	<b>37</b>
4.1	Convergence of the spectral expansion . . . . .	37
4.2	Preliminary considerations . . . . .	39
4.3	Comparison with the experimental spectra . . . . .	43
4.4	Prediction of the current LHC run . . . . .	51
<b>5</b>	<b>Discussion</b>	<b>55</b>
	<b>Glossary</b>	<b>57</b>
	<b>List of Figures</b>	<b>59</b>
	<b>References</b>	<b>61</b>

# Chapter 1

## Introduction

During a heavy-ion collision at the Large Hadron Collider (LHC) or the Relativistic Heavy Ion Collider (RHIC), two highly relativistic nuclei, such as lead or gold, collide, freeing an exceptional amount of energy that fuels a complex cascade of interactions, that finally results in the productions of thousands of particles. These interactions are dominated by the strong force, and heavy-ion collisions offer a unique experimental setup to study Quantum Chromodynamics (QCD) under extreme conditions at non-zero temperature and density. Shortly after the collision, the strongly interacting matter forms a dense deconfined state, the Quark-Gluon Plasma (QGP), that cools down and hadronizes, finally leading to a measured particle shower. This exotic state of matter, where quarks and gluons are deconfined, is believed to be akin to the state of the universe microseconds after its inception, and heavy-ions collisions are the only experimental condition that can reproduce such a phenomenon.

The possibility of probing QCD near its phase transition from the deconfined to the confined state, the possible existence of a critical point of the theory, the conditions of the early universe, and many other fascinating open questions of the physical realm, motivates the growing research in this field.

Since Einstein first provided a theoretical description of Brownian motion based on statistical mechanics [1] in 1905, much progress has been made towards a probabilistic interpretation of particles trajectories [2–6] and a firm mathematical foundation of probability theory and stochastic processes [7–12]. However, only decades after these findings, it was achieved to conciliate stochastic processes with Einstein’s theory of special relativity by incorporating the particle’s momentum in a more general phase-space description [13–15].

Models based on the Fokker-Planck equation (FPE) [16, 17], that, complementary to stochastic calculus, encode the probabilistic nature of a process in the time evolution of its probability density function (PDF), have been widely used in many fields of physics, chemistry, biology and economics. In particle physics, a phenomenological Relativistic Diffusion Model (RDM) based on the FPE has been developed by Wolschin [18] and Biyajima *et al.* [19] to describe the evolution of number den-

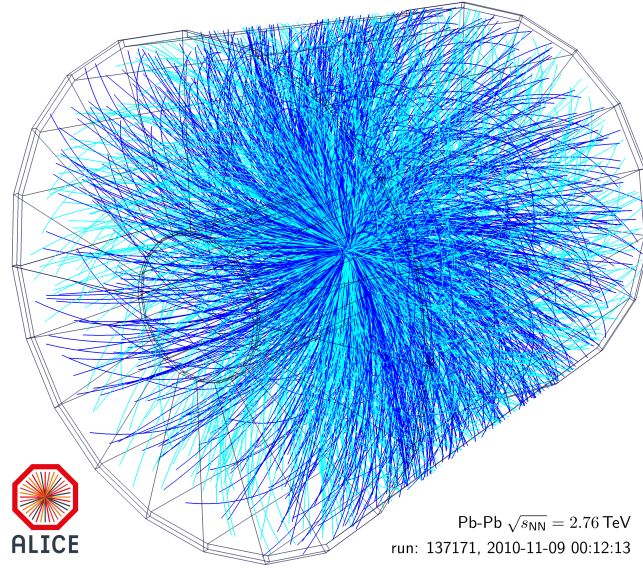


Figure 1.1: Depiction of the particle shower detected at the ALICE experiment generated by a single Pb-Pb central collision at  $\sqrt{s_{NN}} = 2.76$  TeV. 1209 positively-charged (darker tracks) and 1197 negatively-charged (lighter tracks) particles are produced, about 80 percent of which are pions. The curvature of a track is inversely proportional to the momentum of the particle. © CERN.

sities functions (NDF) of different kinds of hadrons in a relativistic heavy-ion collision. While in most of the available theories of relativistic heavy-ion collisions, charged-hadron production is considered to occur from the hot fireball of partons that expands, cools, and eventually hadronizes in a parton-hadron crossover, in a RDM with three sources [20], the highly excited fragments also partake in particle production. Mehtar-Tani & Wolschin [21, 22] accounted for the role of these additional sources, which are clearly visible in net-baryon ("stopping") distributions at the Super Proton Synchrotron (SPS) and RHIC, using a model that relies on gluon-saturation physics. Hoelck & Wolschin [23] have later incorporated this approach in a nonequilibrium statistical model that also accounts for the time-dependence of the stopping process in one effective dimension.

Motivated by the success in describing stopping data from SPS and RHIC, the two aforementioned authors have extended the relativistic diffusion approach to charged hadron thermalization [24] in heavy-ion collisions, where the central fireball becomes the main source of particle production. Similarly to the stopping investigation, the initial state is derived from QCD and evolved in time with a two-dimensional FPE in longitudinal and transverse momentum space constructed via the appropriate fluctuation-dissipation relation (FDR), that connects the drift and diffusion coefficients with the expected asymptotic state. The majority of the produced hadrons participate in the thermalization process, but since the system is not spatially con-



finer, it cannot reach a true thermal equilibrium that is stationary in position space and independent of its initial state. Therefore, the asymptotic PDF is expected to be a modified thermal distribution that exhibits a collective expansion of the system, reminiscent of its initial configuration. Although a correct description of the asymptotic state is crucial in the model to mesoscopically derive the form of the FPE, the system is expected to never complete the thermalization process due to a "freeze out" of interactions, and charged hadrons remain far from equilibrium at the time they are detected. The predictions of this relativistic diffusion model [24] have been successfully compared to LHC spectra in both the longitudinal and transverse direction. However, the accuracy of the finite difference numerical method employed in solving the FPE prevented the comparison to experimental data in a large transverse momentum region, where the particle yield is small compared to the peak of the distribution, but measured with high accuracy.

This thesis aims at improving the accuracy of the model by using a spectral method of solution for solving the partial differential FPE, and therefore obtain meaningful predictions of the charged hadron spectra in a larger phase-space region. This is done employing a spectral eigenfunction decomposition of the associated differential operator, that allows to obtain a solution with a high accuracy on the entire domain of definition.

In Chapter 2, a concise but self-consistent introduction to probability theory and stochastic dynamics is presented, specifically targeted at the scope of this thesis work. It does not aspire to a comprehensive treatment of the subject, but rather to rigorously establish the formalism used in the subsequent chapters. Special attention is reserved to the derivation of the FPE and the discussion of the associated differential operator spectral properties.

Chapter 3 covers the extension to special relativity of stochastic processes, and introduces the physical system of interest, laying the basis of the relativistic drift-diffusion model of heavy-ion collisions. Then, more insights are given for charged hadrons thermalization, and the initial and asymptotic state of such a process are covered in detail. Finally, the explicit spectral method used for solving the derived FPE is discussed.

In Chapter 4, the applicability of the solution method is discussed for the central and fragmentation sources, with strikingly different outcomes in the two cases. It follows a comparison of the model outcome to ALICE [25–27] and ATLAS [28] measurements of Pb-Pb collisions with  $\sqrt{s_{NN}} = 2.76$  and 5.02 TeV, and the free parameters are fixed with a  $\chi^2$  minimization. Lastly, these parameters are extrapolated to  $\sqrt{s_{NN}} = 5.36$  TeV, and a prediction is made for the ongoing LHC run at this energy.

Chapter 5 concludes the thesis with a discussion of the obtained results, desirable

## *Chapter 1. Introduction*

improvements of the model, and future outcomes of the research.

# Chapter 2

## Probability theory and stochastic processes

In many areas of natural and social sciences, and especially in physics, a profound understanding of uncertainty and random behavior is essential for describing and predicting certain natural phenomena. Probability theory and stochastic processes provide the mathematical framework to formulate the physical laws of probabilistic systems. This introduction aims to provide the necessary background to construct the relativistic drift-diffusion model presented in the subsequent chapter. While efforts were made to make it self-consistent, the interested reader is encouraged to consult standard textbooks such as the one by Gardiner [29] and Pavliotis [30], as the report by Hänggi & Thomas [31]. A short and practical course can be found in Schwarz [32] lecture notes and a detailed discussion of the Fokker-Planck equation in the book by Risken [33].

### 2.1 Basis of probability theory

Before studying a stochastic process, it is necessary to introduce the mathematical framework of probability theory. Following the rigorous axiomatic approach by Kolmogorov [11], start by considering the set of all possible outcomes of a measure, the *sample space*  $\Omega$ , that is asked to be *measurable*. An *event*  $A \subseteq \Omega$  is defined as a subset of the sample space and  $\omega \in \Omega$  as a single outcome of the experiment.  $\emptyset$  is the *empty set*, that contains no events.

Using the most classical of examples, if the experiment is throwing an ordinary six-faced dice, the sample space  $\Omega$  would be getting any number from one to six, an event  $A$  getting e.g. an odd number, and  $\omega$  getting a specific number. In the context of this thesis,  $\Omega$  will be the continuous phase space of a relativistic particle measured by a detector at the end of a complex interaction modeled with a stochastic process.

The  $\sigma$ -algebra  $\mathcal{F}$  is the mathematical structure that assigns probabilities to events. It is a collection of subsets of  $\Omega$  that contains the entire sample space and is closed under complementation and countable unions.  $\mathcal{F}$  serves a crucial role in defining the concept of probability, as it restricts which events or sets of outcomes can be assigned probabilities within the sample space  $\Omega$ . For example, when  $\Omega$  is uncountable, not all subsets of the sample space need to be events.

As a relevant physical example, let  $\Omega = \mathbb{R}^n$ . The  $\sigma$ -algebra generated by the open subset (open balls) of  $\mathbb{R}^n$  is called the *Borel  $\sigma$ -algebra*, denoted by  $\mathcal{B}(\mathbb{R}^n)$ . If  $G$  is a closed subset of  $\mathbb{R}^n$ , its Borel  $\sigma$ -algebra  $\mathcal{B}(G)$  is analogously defined.

A *probability measure*  $P$  is a function that assigns a real number in the interval  $[0, 1]$  to each event in the  $\sigma$ -algebra  $\mathcal{F}$ , satisfying the following *probability axioms*:

- i)  $P(A) \geq 0$  for all  $A \in \mathcal{F}$
- ii)  $P(\Omega) = 1$
- iii) If  $A_i (i = 1, 2, 3 \dots)$  is a countable collection of non-overlapping sets,  $A_i \cap A_j = \emptyset$  for all  $i \neq j$ , then

$$P\left(\bigcup_i A_i\right) = \sum_i P(A_i)$$

From these three fundamental axioms, it follows:

- iv) if  $\bar{A}$  is the complement of  $A$ , i.e., the set of all events not contained in  $A$ , then

$$P(\bar{A}) = 1 - P(A),$$

- v)  $P(\emptyset) = 0$

The axiomatic construction of probability, while providing a solid formal mathematical framework, requires that the *probability space*  $(\Omega, \mathcal{F}, P)$  is defined, with the probability measure  $P$  assigned *a priori*. These *a priori probabilities* are simply assumed, e.g. when one assigns equal probabilities to equal volumes of the phase space in equilibrium statistical mechanics.

## 2.2 Random variables and probability distributions

To describe a physical stochastic process, a mathematical representation of probabilistic quantities is necessary. A *stochastic* or *random variable*  $X$  is a *measurable*

*function* of an experiment's outcome, i.e. a map  $X(\omega)$  from  $(\Omega, \mathcal{F}, P)$  to some measurable space  $(E, \mathcal{G})$  called the *state space*, in this thesis typically  $\mathbb{R}$  or  $\mathbb{R}^+$  equipped with a Borel algebra.  $X$  can randomly take some value  $x$ , in what is called a *realization*.

In a simple but frequent case,  $x$  and  $\omega$  coincide. For example, the position and momentum of a particle can be thought of as being both part of the event space and the observed random variable. In this instance, the argument of  $X$  is usually omitted. On the contrary, in the case e.g. of a complex system like a fluid,  $\omega$  could contain information about the positions and momenta of every single particle, while  $x$  could be the realization of some macroscopic random variable  $X(\omega)$  such as the density or pressure of the liquid.

The probability that the realization of  $X$  is contained in some subset  $G$  of the state space  $E$  is:

$$P_X(G) := P[X \in G] = \int_G dP_X, \quad G \in \mathcal{B}(E), \quad (2.1)$$

where  $P_X^1$  is the probability measure associated with  $X$ , also called the *distribution* or *law* of  $X$ . The *expectation* of a function  $h(X)$  is defined as:

$$\mathbb{E}[h(X)] := \int_E h dP_X \quad (2.2)$$

Equations (2.1) and (2.2) are valid for both discrete and continuous random variables, and the Lebesgue integral in them can be reduced to a finite sum or a Riemann integral.

### 2.2.1 Probability mass and density functions

The knowledge of  $P_X(G)$  for every subset  $G \in \mathcal{B}(E)$  is sufficient to have a complete description of the random variable  $X$ . However, since a random variable may assume an infinite number of possible realizations, a description in terms of all possible subsets of the event space, while mathematically elegant, is unpractical. To handle random variables more easily, an equivalent probability function can be defined, that requires only a single element of the event space as an argument. This function can be derived from  $P_X$  for discrete and continuous variables as follows:

A random variable  $X$  with values on  $\mathbb{R}$  is called *discrete* if it takes values in some *countable* subset  $\{x_0, x_1, x_2, \dots\}$  of  $\mathbb{R}$ . Then, the integral in equation (2.1) can be written as a countable sum:

$$P_X(G) = \sum_{x \in G} P_X(\{x\}) = \sum_{x \in G} p_X(x), \quad (2.3a)$$

---

<sup>1</sup>To have a compact but univocal notation, we will indicate with a  $P$  without subscripts a general probability of some event to happen, with  $P_X$  without argument the probability measure of  $X$  and with  $P_X(G)$  the probability that  $X \in G$ .

where the *probability mass function* (PMF)  $p_X(x) := P_X(\{x\})$  is defined. The expectation of a function  $h$  on the state space  $E$ , eq. (2.2), accordingly becomes

$$\mathbb{E}[h(X)] = \sum_{x \in E} h(x)p_X(x). \quad (2.3b)$$

A random variable  $X$  with values on  $\mathbb{R}$  is called *continuous* if  $P(X = x) = 0$  for all  $x \in \mathbb{R}$ . If the probability measure  $P_X$  is absolutely continuous with respect to the Lebesgue measure with density  $f_X$ , i.e.  $P_X(dx) = f_X(x)dx$ , the probability  $P_X(G)$  can be written as

$$P_X(G) = \int_G dP_X = \int_G f_X(x)dx. \quad (2.4a)$$

$f_X := dP_X/dx$  is called the *probability density function* (PDF). The expectation (2.2) takes the form:

$$\mathbb{E}[h(X)] = \int_E h(x)f_X(x)dx. \quad (2.4b)$$

For a  $n$ -dimensional stochastic variable  $\mathbf{X}$  on  $\mathbb{R}^n$ , with  $\mathbf{x} = (x^1, \dots, x^n)$  and  $d^n x = \prod_{i=1}^n dx^i$ , eq (2.4a) becomes

$$P_{\mathbf{X}}([\mathbf{x}, \mathbf{x} + d\mathbf{x}]) = f_{\mathbf{X}}(\mathbf{x})d^n x. \quad (2.4c)$$

One of the most fundamental tools when solving a physics problem is choosing an adapt set of coordinates, thus it is necessary to be able to perform stochastic changes of variables. Let  $\mathbf{X}$  be a  $n$ -dimensional continuous random variable on the event space  $E$ , and  $\varphi$  a diffeomorphism  $E$  as its domain. Then,  $\mathbf{Y} = \varphi(\mathbf{X})$  is also a  $n$ -dimensional continuous random variable, and the PDFs of  $\mathbf{X}$  and  $\mathbf{Y}$  are connected through the determinant of the Jacobian of  $\varphi$ :

$$f_{\mathbf{X}}(\mathbf{x}) = |\det(\mathbf{J}_{\varphi}(\mathbf{x}))|f_{\mathbf{Y}}(\mathbf{y}) \quad (2.5)$$

to characterize a probability distribution, useful quantities are the *moments*  $\langle \mathbf{X}^m \rangle = \mathbb{E}[\mathbf{X}^m]$ . In particular, the *mean*  $\boldsymbol{\mu} \in \mathbb{R}^n$  and the *covariance*  $\boldsymbol{\Sigma} \in \mathbb{R}^{n \times n}$  are the quantities:

$$\boldsymbol{\mu} = \mathbb{E}[\mathbf{X}], \quad \boldsymbol{\Sigma} = \mathbb{E}[(\mathbf{X} - \boldsymbol{\mu})(\mathbf{X} - \boldsymbol{\mu})^T]. \quad (2.6)$$

The diagonal of  $\boldsymbol{\Sigma}$  is called the *variance*  $\boldsymbol{\sigma}$  of  $\mathbf{X}$ .

A  $n$ -dimensional continuous real random variable is *Gaussian* or *normally distributed* with mean  $\boldsymbol{\mu}$  and covariance  $\boldsymbol{\Sigma}$ , in short

$$\mathbf{X} \sim \mathcal{N}(\boldsymbol{\mu}, \boldsymbol{\Sigma}), \quad (2.7)$$

if its PDF is of the form:

$$f_{\mathbf{X}} = \frac{1}{\sqrt{(2\pi)^n \det \Sigma}} \exp \left( -\frac{1}{2} (\mathbf{x} - \boldsymbol{\mu})^T \Sigma^{-1} (\mathbf{x} - \boldsymbol{\mu}) \right). \quad (2.8)$$

Any linear transformation  $\mathbf{Y} = \mathbf{A}\mathbf{X} + \mathbf{b}$  of a normally distributed random variable, with  $\mathbf{A} \in \mathbb{R}^{m \times n}$  and  $\mathbf{b} \in \mathbb{R}^m$ , is also normally distributed:

$$\mathbf{Y} \sim \mathcal{N}(\mathbf{A}\boldsymbol{\mu} + \mathbf{b}, \mathbf{A}\Sigma\mathbf{A}^T). \quad (2.9)$$

Normally distributed random variables play a crucial role in probability theory and stochastic dynamics, as many stochastic processes asymptotically approach a Gaussian distribution. The *central limit theorem* states that the sequence of centered independent identically distributed random variables  $Y_n = X_n - V$ , with  $\mathbb{E}[X] = V$  and  $\mathbb{E}[(X - V)^2] = \sigma^2$ , approaches a normal distribution:

$$\lim_{n \rightarrow \infty} \frac{1}{\sigma\sqrt{N}} \sum_{n=1}^N Y_n \sim \mathcal{N}(0, 1). \quad (2.10)$$

### 2.2.2 Independence, joint and conditional probability

Informally, two random variables are *independent* if the realization of one does not affect the probability distribution of the other. Formally, two random variables  $X, Y$  from  $\Omega$  to  $\mathbb{R}$  are independent *if and only if*, for all  $x, y \in \mathbb{R}$ , the events  $\{\omega \in \Omega | X(\omega) \leq x\}$  and  $\{\omega \in \Omega | Y(\omega) \leq y\}$  are *independent events*, that is:

$$P(A \cap B) = P(A)P(B). \quad (2.11)$$

Let  $X$  from  $\Omega'$  to  $S'$  and  $Y$  from  $\Omega''$  to  $S''$  be two random variables. They can be considered a random vector  $\mathbf{Z} = (X, Y)$  from  $\Omega = \Omega' \otimes \Omega''$  to  $S = S' \otimes S''$ . Let  $\mathcal{X}, \mathcal{Y}$  be two subsets of  $S'$  and  $S''$  respectively. Then, when explicating the two components, the probability that  $\mathbf{Z} \in \mathcal{Z} = \mathcal{X} \otimes \mathcal{Y}$  is referred to as the *joint* probability of  $X \in \mathcal{X}$  and  $Y \in \mathcal{Y}$ :

$$P_{X,Y}(\mathcal{X}, \mathcal{Y}) := P_{\mathbf{Z}}(\mathcal{Z}) = \int_{\mathcal{X}, \mathcal{Y}} dP_{X,Y} = \int_{\mathcal{Z}} dP_{\mathbf{Z}}. \quad (2.12)$$

In the case of continuous variables, if the mixed derivative of  $P_{X,Y}$  exists, it is called the joint PDF of  $X$  and  $Y$ :

$$f_{X,Y}(x, y) = \frac{d^2 P_{X,Y}(x, y)}{dx dy}. \quad (2.13)$$

If the interest is only in one of the components of the random vector, say in  $X$ , then the *marginal* probability that  $X \in \mathcal{X}$  irrespective of the realization of  $Y$  is

$$P_X(\mathcal{X}) = P_{X,Y}(\mathcal{X}, S''). \quad (2.14)$$

When they exist, the marginal and joint PDF are related by

$$f_X(x) = \int_y f_{X,Y}(x, y) dy. \quad (2.15)$$

A necessary and sufficient condition for two random variables to be independent is that their joint probability is the product of the two marginal probabilities:

$$P_{X,Y}(\mathcal{X}, \mathcal{Y}) = P_X(\mathcal{X})P_Y(\mathcal{Y}), \quad f_{X,Y}(x, y) = f_X(x)f_Y(y). \quad (2.16)$$

If, on the contrary, the focus is on how the realization of one variable conditions the probability distribution of the other, the appropriate information is contained in the *conditional* probability

$$P_{X|Y}(\mathcal{X}|\mathcal{Y}) := \frac{P_{X,Y}(\mathcal{X}, \mathcal{Y})}{P_Y(\mathcal{Y})}, \quad (2.17)$$

as the probability that  $X \in \mathcal{X}$  given that  $Y \in \mathcal{Y}$ . If  $\mathcal{Y} = S''$ , i.e. no information about the realization of  $Y$  is included, eq. (2.17) reduces to eq. (2.14). Analogously, the conditional PDF is

$$f_{X|Y}(x|y) = \frac{f_{X,Y}(x, y)}{f_Y(y)}. \quad (2.18)$$

Generalization of formulas (2.15) and (2.18) to the PMF of discrete variables is straightforward. Generalization to more than two variables is also straightforward since all the formulas in this subsection are valid if  $X$  and  $Y$  are substituted with multidimensional stochastic variables  $\mathbf{X}$  and  $\mathbf{Y}$ .

## 2.3 Stochastic processes

Now that a mathematical representation of probabilistic systems with stochastic variables and their probability distributions is established, it is possible to study the probabilistic time evolution of such a system.

A *stochastic process* is a collection of random variables  $\mathbf{X} = \{\mathbf{X}_t; t \in T\}$ , where  $T$  is an *ordered set*, and for each  $t \in T$ , a *member*  $\mathbf{X}_t$  is a random variable from the same probability space  $(\Omega, \mathcal{F}, P)$  to the same measurable space  $(E, \mathcal{G})$ . The *parameter set*  $T$  can be countable or connected, and the stochastic process  $\mathbf{X}$  is respectively called *parameter-discrete* or *parameter-continuous*. If every member of the process is a discrete (continuous) random variable,  $\mathbf{X}$  is referred to as *value-discrete* (*continuous*). A stochastic process can be also viewed as a function of both  $t \in T$  and  $\omega \in \Omega$ . For a fixed sample point  $\omega$ , the function  $\mathbf{X}_t(\omega) = \mathbf{X}(\omega, t) : T \rightarrow E$  is called a *path*, *trajectory* or *realization* of the process  $\mathbf{X}$ .

The mathematical treatment of a stochastic process can be quite challenging when the parameter set is not discrete, e.g. in the case of the continuous-time evolution of a probabilistic system. A great simplification comes into play when one only considers processes that possess the *Markov property* [7].



### 2.3.1 Markov processes

If the parameter set  $T$  is *totally ordered*, such that the members of the stochastic process  $\mathbf{X}$  can be arranged in a sequence  $\{\mathbf{X}(t)\}_{t \in T}$  of stochastic variables, and each member  $\mathbf{X}(t)$  depends only on a number of predecessors smaller than a finite  $m \in \mathbb{N}$ , then  $\mathbf{X}$  is a *Markov process of order  $m$* . If  $t$  has the meaning of a time, then Markov processes can be said to have a "short-term memory". In particular, for a Markov process of order one, given the present, the past and the future are statistically independent.

The following discussion is restricted to the latter case of order  $m = 1$ , since any higher-order process  $\mathbf{X}$  of dimension  $n$  and order  $m$  can be rewritten into a  $(nm)$ -dimensional first-order Markov process  $\mathbf{Y}$ . For a time-discrete process, this can be done by defining

$$\mathbf{Y}(t_k) := (\mathbf{X}(t_k), \mathbf{X}(t_{k-1}), \dots, \mathbf{X}(t_{k-m+1})), \quad (2.19a)$$

while in case of a time-continuous process with infinitesimal distance  $dt$  between the elements of  $T$ , it is achieved by

$$\mathbf{Y}^i(t) := \sum_{k=1}^i (-1)^k \binom{i}{k} \frac{\mathbf{X}(t - kdt)}{(dt)^k} := \frac{\partial^i \mathbf{X}(t)}{\partial t^i}, \quad i = 1, \dots, m. \quad (2.19b)$$

The possibility of rewriting a stochastic process in the form (2.19b) can be considered the defining property of time-continuous Markov processes of order  $m$ .

The fact that a higher order process can be rewritten in terms of its  $m - 1$  derivatives to obtain a higher dimensional first-order process is similar to how an ordinary differential equation (ODE) of order  $m$  is equivalent to a system of  $m$  coupled ODEs. In fact, the main result of this section will be to derive equations of motion for stochastic processes in the form of *stochastic differential equations*.

To understand how the Markov property simplifies the treatment of a stochastic process  $\mathbf{X}$ , divide its parameter set  $T$  into  $n$  segments  $T_k$  such that  $\bigcup_{k=1}^n T_k = T$ , and if  $i < j$ , then  $t_i < t_j$  for all  $t_i \in T_i, t_j \in T_j$ . Then, the probability that  $\mathbf{X} = (\mathbf{X}_1, \dots, \mathbf{X}_n)$ , where  $\mathbf{X}_k = (\mathbf{X}(t) | t \in T_k)$ , takes a path in  $S = \otimes_{k=1}^n S_k$  can be written applying recursively eq. (2.17) as

$$P_{\mathbf{X}}(S) = P_{\mathbf{X}_1}(S_1) \prod_{k=1}^{n-1} P_{\mathbf{X}_{k+1}|\mathbf{X}_k}(S_{k+1}|S_k), \quad (2.20)$$

since the Markov property guarantees that  $\mathbf{X}_{k+1}$  depends directly on only his immediate predecessor  $\mathbf{X}_k$ :

$$P_{\mathbf{X}_{k+1}|\mathbf{X}_1, \dots, \mathbf{X}_k}(S_{k+1}|S_1 \otimes \dots \otimes S_k) = P_{\mathbf{X}_{k+1}|\mathbf{X}_k}(S_{k+1}|S_k) \quad (2.21)$$

Equation (2.20) means that a stochastic process  $\mathbf{X}$  is completely specified by the initial state  $\mathbf{X}_1$  and the *two-point* conditional probability  $P_{\mathbf{X}_{k+1}|\mathbf{X}_k}$ , also called *transitional probability* or *propagator* from one state to the next. Assuming that the process  $\mathbf{X}$  is time- and value-continuous, and that PDFs exists for every  $\mathbf{X}(t)$ , then from eq (2.20) it follows that

$$f(\mathbf{x}_1, t_1, \dots, \mathbf{x}_n, t_n) = f(\mathbf{x}_1, t_1) \prod_{k=1}^{n-1} f(\mathbf{x}_{k+1}, t_{k+1} | \mathbf{x}_k, t_k), \quad (2.22)$$

where  $t_1 < \dots < t_n$ <sup>2</sup>. Using these properties of Markov processes, a formula for the transition from arbitrary points can be derived:

$$f(\mathbf{x}, t_3 | \mathbf{y}, t_1) = \int_{\mathbb{R}^d} f(\mathbf{x}, t_3 | \mathbf{z}, t_2) f(\mathbf{z}, t_2 | \mathbf{y}, t_1) d^d z, \quad (2.23)$$

where  $t_1 < t_2 < t_3$ . This is the *Chapman-Komogorov equation* [9, 10] for the *transition probability density*. It is a nonlinear functional equation relating all transition probabilities to each other, and its differential form is at the basis of *stochastic differential equations* (SDE).

In the next two subsections, the two perhaps most simple and commonly found Markov processes are presented as examples.

### 2.3.2 The Random walk and the Wiener process

A *symmetric random walk* on a line is a time- and value-discrete first-order Markov process  $R$  that starts at a particular position  $R(t_0) = R_0$ , and at each time step, jumps a positive distance  $\Delta r$  either to the left or to the right with equal probability. The position  $R(t_n)$  after  $n$  steps can be represented as

$$R(t_n) = R_0 + \sum_{i=1}^n X_i, \quad (2.24a)$$

where  $X_i = \pm \Delta r$  is a random variable representing the  $i$ -th jump, with PMF

$$p_{X_i}(r) = \frac{1}{2} \delta(r - \Delta r) + \frac{1}{2} \delta(r + \Delta r), \quad \forall i = 1, \dots, n. \quad (2.24b)$$

With some combinatorics, it can be shown that the probability of the process to be at position  $m\Delta r$  after  $N$  jumps starting at  $R_0 = 0$  is

$$p_R(m\Delta r, t_N) = \frac{N!}{2^N \left(\frac{N-m}{2}\right)! \left(\frac{N+m}{2}\right)!} \quad (2.24c)$$

if  $\frac{N-m}{2} \in \mathbb{N}_0$ , and null otherwise. The average position is  $\mathbb{E}[R(t_N)] = 0$  and the variance is  $\mathbb{E}[R^2(t_N)] = N$ .

---

<sup>2</sup>For compactness, subscripts or the time argument can be omitted:  $f_{\mathbf{X}(t_1)|\mathbf{X}(t_2)}(\mathbf{x}_1, t_1 | \mathbf{x}_2, t_2) = f(\mathbf{x}_1, t_1 | \mathbf{x}_2, t_2) = f_{\mathbf{X}(t_1)|\mathbf{X}(t_2)}(\mathbf{x}_1 | \mathbf{x}_2)$ , and analogously for joint PDF.

The *standard Wiener process* [8] is a continuous-time stochastic process that models e.g. the random Brownian motion of particles suspended in a fluid or Gaussian noise. A Wiener process  $W$  is characterized by the following properties:

1. The initial condition is  $W(0) = 0$ ;
2. For any  $0 \leq t_1 < \dots < t_n$ , the random variables  $W(t_1), \dots, W(t_n) - W(t_{n-1})$  are independent and normally distributed with mean zero and variance  $\Delta t = t_i - t_{i-1}$ ;
3. It exhibits continuous sample paths.

From the second and third properties, it follows that  $dW(t) \sim \mathcal{N}(0, dt)$ . The transition PDF can be identified with the marginal probability of an increment of  $W$ :

$$f_{W_t|W_{t+\Delta t}}(w + \Delta w|w) = f_{W_{t+\Delta t}-W_t}(\Delta w) = \frac{1}{\sqrt{2\pi\Delta t}} \exp\left(-\frac{(\Delta w)^2}{2\Delta t}\right), \quad (2.25a)$$

for any positive  $\Delta t$ . Furthermore, because of the first requirement,

$$W(t) \sim \mathcal{N}(0, t). \quad (2.25b)$$

The Wiener process is an example of *time-homogeneous* Markov process, that is, its transition probability  $f_{W_t|W_{t+\Delta t}}$  depends only on the time difference  $\Delta t$ , as seen in equation (2.25a).  $W(t)$  is continuous in  $t$ , but nowhere differentiable. The *functional central limit theorem* states that the Wiener process can be constructed as the scaling limit of a random walk [34].

### 2.3.3 Diffusion processes

A *drift-diffusion process* is a Markov process that has continuous sample paths, i.e. a Markov process without jumps. An  $n$ -dimensional drift-diffusion process  $\mathbf{X}$  with smooth Lipschitz-continuous drift  $\boldsymbol{\mu}_{\mathbf{X}}(\mathbf{x}, t) \in \mathbb{R}^n$  and diffusion  $\boldsymbol{\sigma}_{\mathbf{X}}(\mathbf{x}, t) \in \mathbb{R}^{n \times m}$  coefficient functions is a time- and value-continuous stochastic process that fulfills the SDE:

$$d\mathbf{X}(t) = \boldsymbol{\mu}_{\mathbf{X}}(\mathbf{x}, t)dt + \boldsymbol{\sigma}_{\mathbf{X}}(\mathbf{x}, t)d\mathbf{W}(t), \quad (2.26a)$$

or, component-wise for  $i = 1, \dots, n$ ,

$$dX^i(t) = \mu_{\mathbf{X}}^i(\mathbf{x}, t)dt + \sum_{l=1}^m \sigma_{\mathbf{X}}^{il}(\mathbf{x}, t)dW^l(t), \quad (2.26b)$$

for a collection of  $m$  independent standard Wiener processes  $\mathbf{W} = (W^1, \dots, W^m)$ . It can be shown that  $\mathbf{X}$  inherits many of the special characteristics of the Wiener processes, especially a normal distribution of infinitesimal increments,

$$d\mathbf{X}(t) \sim \mathcal{N}(\boldsymbol{\mu}_{\mathbf{X}}dt, 2\mathbf{D}_{\mathbf{X}}dt), \quad (2.27)$$

where  $\mathbf{D}_{\mathbf{X}}(\mathbf{x}, t) := \frac{1}{2} \boldsymbol{\sigma}_{\mathbf{X}} \boldsymbol{\sigma}_{\mathbf{X}}^{\top} \in \mathbb{R}^{n \times n}$  denotes the *diffusivity* of  $\mathbf{X}$ , and that the conditional PDF fulfills

$$f_{\mathbf{X}(t+dt)|\mathbf{X}(t)}(\mathbf{x} + d\mathbf{x} \mid \mathbf{x}) = f_{\mathbf{X}(t+d)-\mathbf{X}(t)}(d\mathbf{x}). \quad (2.28)$$

To obtain finite increments, one has to formally integrate eq. (2.26a), making use of *stochastic integrals*. To carry out this formal integration, a *discretization rule* must first be specified. Here we will not give details, but we will briefly mention the two most common discretization rules found in the literature and their properties.

The pre-point rule leads to the *Itô integral* [12], while the mid-point rule defines the *Stratonovich-Fisk integral* [35, 36]. In contrast to Riemann integration, stochastic integrals do not converge independently of the discretization, thus, when integrating eq. (2.26a), the result depends on the discretization scheme adopted. The different schemes also impact the substitutions of variables into the integration, and consequently changes of variables of the stochastic process. Standard rules of calculus are retrieved for the Stratonovich-Fisk integral, while with Itô calculus anomalous extra terms appear. However, the latter discretization scheme is well suited for numerical simulations and is the mathematically best understood, with many theorems proved only for this choice.

The stochastic integrals obtained from different discretization rules can be connected by a suitable change in the drift and diffusion coefficients. That means, that once a scheme is set, the same stochastic process can be described by changing the coefficients accordingly. In other words, the choice of discretization does not alter  $\mathbf{X}$ , but only its representation in terms of coefficient functions: this fact is referred to as discretization freedom.

## 2.4 The Fokker-Planck equation

This section proceeds to obtain a differential equation for the time evolution of the probability distribution, which will eventually be the equation used to describe drift-diffusion processes in this thesis. Then, it outlines its main properties and illustrates some crucial results about its solution in the one- and multi-dimensional case. Finally, the last subsection presents a simple but illustrative example. The interested reader is referred to the book by Risken [33], where rigorous proofs and derivations are given.

### 2.4.1 The Kramers-Moyal expansion

Here, a short derivation of the one-dimensional FPE is given. The multi-dimensional equation is simply stated in the subsequent subsection. From the definition of conditional probability, it follows that the PDFs  $f_{\mathbf{X}(t+\tau)}(x)$  at time  $t + \tau$  and  $f_{\mathbf{X}(t)}(x)$

at time  $t$  are connected by

$$f_{X(t+\tau)}(x) = \int f_{X(t)|X(t+\tau)}(x|x') f_{X(t)}(x') dx', \quad (2.29)$$

for  $\tau \geq 0$ . Using a formal Taylor expansion of the  $\delta$ -function, their difference can be written as

$$f_{X(t+\tau)}(x) - f_{X(t)}(x) = \sum_{n=1}^{\infty} \left( -\frac{\partial}{\partial x} \right)^n \frac{M_n(x, t, \tau)}{n!} f_{X(t)}(x), \quad (2.30a)$$

where the  $M_n$  are the moments of the transition density:

$$M_n(x', t, \tau) = \int (x - x')^n f_{X(t)|X(t+\tau)}(x|x') dx. \quad (2.30b)$$

Suppose now that the moments can be expanded into a Taylor series with respect to  $\tau$ :

$$\frac{M_n(x, t, \tau)}{n!} = D^{(n)}(x, t) \tau + \mathcal{O}(\tau^2). \quad (2.30c)$$

Then, by taking into account only linear terms in  $\tau$ , the time derivative of the PDF is given by the *Kramers-Moyal forward expansion* [37, 38]:

$$\frac{\partial f_X(x, t)}{\partial t} = \sum_{n=1}^{\infty} \left( -\frac{\partial}{\partial x} \right)^n D^{(n)}(x, t) f_X(x, t) = L_{\text{KM}} f_X(x, t), \quad (2.31a)$$

where the derivatives act on  $D^{(n)}(x, t)$  and  $f_X(x, t)$ , and  $L_{\text{KM}}$  is the Kramers-Moyal operator

$$L_{\text{KM}}(x, t) = \sum_{n=1}^{\infty} \left( -\frac{\partial}{\partial x} \right)^n D^{(n)}(x, t). \quad (2.31b)$$

If the expansion stops at the second coefficient, the one-dimensional *Fokker-Planck equation* (FPE) [16, 17], is retrieved, also known as the *forward Kolmogorov equation*:

$$\frac{\partial f_X(x, t)}{\partial t} = L_X f_X(x, t), \quad (2.32a)$$

where

$$L_X(x, t) = -\frac{\partial}{\partial x} D^{(1)}(x, t) + \frac{\partial^2}{\partial x^2} D^{(2)}(x, t) \quad (2.32b)$$

is the *Fokker-Planck operator* (FPO).

### 2.4.2 The Fokker-Planck equation in diffusion processes

For a  $n$ -dimensional drift-diffusion process  $\mathbf{X}$ , the truncation of the Kramers-Moyal expansion at the second term is exact, and the FPE can be expressed in terms of the drift vector  $\boldsymbol{\mu}_{\mathbf{X}}$  and the diffusion matrix  $\mathbf{D}_{\mathbf{X}}$  as

$$\frac{\partial f_{\mathbf{X}}}{\partial t} = L_{\mathbf{X}} f_{\mathbf{X}}, \quad (2.33a)$$

$$L_{\mathbf{X}}(\mathbf{x}, t) = -\frac{\partial}{\partial x^i} \mu_{\mathbf{X}}^i(\mathbf{x}, t) + \frac{\partial^2}{\partial x^i \partial x^j} D_{\mathbf{X}}^{ij}(\mathbf{x}, t), \quad (2.33b)$$

where Einstein's notation for implicitly summing on repeated indices was used. This is a linear parabolic partial differential equation with formal solution

$$f_{\mathbf{X}}(\mathbf{x}, t) = e^{(t-t')L_{\mathbf{X}}} f_{\mathbf{X}}(\mathbf{x}, t'), \quad t > t'. \quad (2.34)$$

Then,  $f_{\mathbf{X}(t_1)}$  is completely determined by an initial condition  $f_{\mathbf{X}(t_0)}$ , the values of the coefficient functions and the value of  $f_{\mathbf{X}(t)}$  at the boundaries for every time  $t_0 < t < t_1$ . That means that the FPE completely characterizes the stochastic process  $\mathbf{X}$ .

The multidimensional FPE (2.33a) with (2.33b) can be written in the form of a continuity equation

$$\frac{\partial f_{\mathbf{X}}}{\partial t} + \frac{\partial S^i}{\partial x^i} = 0, \quad (2.35a)$$

with the probability density current  $S^i$  defined as

$$S^i = \mu_{\mathbf{X}}^i f_{\mathbf{X}} - \frac{\partial}{\partial x^j} D_{\mathbf{X}}^{ij} f_{\mathbf{X}}. \quad (2.35b)$$

If the probability current vanishes at the boundaries, then eq. (2.35a) guarantees that the total probability remains constant.

If the coefficient functions do not depend explicitly on time, then the existence of a stationary solution is expected. In the one-dimensional case, the probability current  $S$  eq. (2.35b) must be constant for stationary solutions. If  $S$  vanishes at the boundaries, then  $S = 0$  everywhere, and eq. (2.35b) can be integrated to get

$$f_{X_{\text{eq}}}(x) = \frac{N}{D_X(x)} \exp\left(\int^x \frac{\mu_X(x')}{D_X(x')} dx'\right) = N e^{-\Phi(x)}, \quad (2.36a)$$

where  $N$  is an integration constant determined by the normalization and  $\Phi$  is the potential

$$\Phi(x) = \ln D_X(x) - \int^x \frac{\mu_X(x')}{D_X(x')} dx'. \quad (2.36b)$$

For the rest of this discussion, natural boundary conditions will always be assumed, which is the case of interest in the relevant stochastic process described in the next chapter. Naturally, other boundary conditions may in general occur, and then eq. (2.36a) must include another term accounting for a finite value of  $S$ .

### 2.4.3 Detailed balance and fluctuation-dissipation relations

In the higher-dimensional case, the probability current is generally not constant in the stationary state, therefore finding an equilibrium solution can be challenging. However, there are certain conditions, called *detailed balance*, under which an

equilibrium solution can be derived similarly as done in one dimension. If this condition is met, for a stationary solution the probability current vanishes, and for an invertible diffusion matrix the potential  $\Phi$  can be defined through a line integral:

$$f_{\mathbf{X}_{\text{eq}}}(\mathbf{x}) = N e^{-\Phi(\mathbf{x})}, \quad \Phi(\mathbf{x}) = \int^{\mathbf{x}} A_{\mathbf{X}}^i(\mathbf{x}) dx^i, \quad (2.37a)$$

where

$$A_{\mathbf{X}}^i := (D_{\mathbf{X}}^{-1})^{ij} \left( \frac{\partial D_{\mathbf{X}}^{jk}}{\partial x^k} - \mu_{\mathbf{X}}^j \right) \quad (2.37b)$$

must satisfy the *potential conditions*

$$\frac{\partial A_{\mathbf{X}}^i}{\partial x^j} = \frac{\partial A_{\mathbf{X}}^j}{\partial x^i}. \quad (2.38)$$

If the stationary solution is known, the function coefficients can be obtained via the *fluctuation-dissipation relations* (FDRs)

$$\mu_{\mathbf{X}}^i f_{\mathbf{X}_{\text{eq}}} = \frac{\partial}{\partial x^k} \left[ D_{\mathbf{X}}^{ik} f_{\mathbf{X}_{\text{eq}}} \right]. \quad (2.39)$$

In the special case of a diagonal constant diffusion matrix  $D_{\mathbf{X}}^{ij} = D_i \delta^{ij}$ , the detailed balance condition is equivalent to the potential condition

$$D_i \frac{\partial \mu_{\mathbf{X}}^i}{\partial x^j} = D_j \frac{\partial \mu_{\mathbf{X}}^j}{\partial x^i}, \quad (2.40)$$

and the FDRs take the simple form

$$\mu_{\mathbf{X}}^i(\mathbf{x}) = D_i \frac{\partial \ln f_{\mathbf{X}_{\text{eq}}}(\mathbf{x})}{\partial x^i}. \quad (2.41)$$

#### 2.4.4 Eigenfunction expansion

For many physical applications, more interesting than knowing the equilibrium state is finding non-stationary solutions of the FPE, and the method used in this thesis to do so is a spectral eigenfunction expansion. This subsection illustrates the theoretical concepts that justify such a solution strategy, while the practical numerical algorithm is explained in chapter 3.

Making a separation ansatz for the non-stationary solution of the type

$$f_{\mathbf{X}}(\mathbf{x}, t) = \varphi(\mathbf{x}) e^{-\lambda t}, \quad (2.42)$$

leads to

$$\mathbf{L}_{\mathbf{X}} \varphi = -\lambda \varphi, \quad (2.43)$$

where  $\varphi(\mathbf{x})$  and  $\lambda$  are the eigenfunctions and eigenvalues of the FPO. To make considerations about its spectrum, it is instructive to take a step back to the

one-dimensional situation first. For an one-dimensional drift-diffusion process, the FPO (2.32a) can be expressed using the potential  $\Phi$  from eq. (2.36b) as

$$L_X(x) = \frac{\partial}{\partial x} D_X(x) e^{-\Phi(x)} \frac{\partial}{\partial x} e^{\Phi(x)}, \quad (2.44)$$

which is clearly not a Hermitean operator. However, by multiplying on the left the FPO by  $e^\Phi$  it can be checked that

$$(e^\Phi L_X)^+ = L_X^+ e^\Phi = e^\Phi L_X. \quad (2.45)$$

Then  $e^\Phi L_X$  is an Hermitean operator, as well as

$$G_X = e^{\Phi/2} L_X e^{-\Phi/2}. \quad (2.46)$$

Assuming for simplicity a discrete spectrum of eigenvalues, if  $\varphi_n(x)$  are the eigenfunctions of the FPO  $L_X$  with eigenvalues  $\lambda_n$ , then the functions

$$\psi_n(x) = e^{\Phi(x)/2} \varphi_n(x) \quad (2.47)$$

are the eigenfunctions of  $G_X$  with the same eigenvalues  $\lambda_n$ . Since  $G_X$  is a Hermitean operator, the eigenvalues are real, and eigenfunctions with different eigenvalues are orthogonal. For normalized eigenfunctions, the orthonormality relation

$$\int \psi_n \psi_m dx = \int e^\Phi \varphi_n \varphi_m dx = \delta_{nm} \quad (2.48)$$

holds. It can be easily checked that all  $\lambda_n \geq 0$ , and that the equality holds only for the stationary solution

$$\varphi_0(x) = \sqrt{N} e^{-\Phi(x)} = \frac{1}{\sqrt{N}} f_{X_{\text{eq}}}(x); \quad \lambda_0 = 0. \quad (2.49)$$

From the positivity of the eigenvalues, it follows that any solution converges exponentially in time to the stationary distribution, as already hinted by the formal solution (2.34). This is a general result holding for the multi-dimensional case as well [39].

Generally, the multi-dimensional FPO (2.33b) cannot be brought into a Hermitean form. If the stationary distribution and thus the potential  $\Phi(\mathbf{x})$  are known, proceeding as in the one-dimensional case leads to the finding that  $G_{\mathbf{X}}$  can be decomposed into the sum of a Hermitean operator  $G_H$  and an anti-Hermitean operator  $G_A$ :

$$G_{\mathbf{X}} = e^{\Phi/2} L_{\mathbf{X}} e^{-\Phi/2} = G_H + G_A. \quad (2.50)$$

While every operator can be decomposed into a Hermitean and a non-Hermitean part, eq. (2.50) is special because applying the square root of the stationary distribution  $e^{-\Phi/2}$  to  $G_H$  or  $G_A$  leads to zero. Moreover, if the detailed balance condition is fulfilled,  $G_A$  vanishes, and  $G_{\mathbf{X}}$  is then a Hermitean operator whose eigenvalues have the same nice properties as in the one-dimensional case.



### 2.4.5 The Ornstein-Uhlenbeck process

The *Ornstein-Uhlenbeck process* [6] was introduced to describe the Brownian motion of particles in velocity space. It is characterized by a linear drift term and by a constant diffusivity  $D > 0$ , and for a one-dimensional process  $U$ , the FPE reads

$$\frac{\partial f_U(v, t)}{\partial t} = \frac{\partial}{\partial v} \left[ \frac{v}{\tau} f_U(v, t) + D \frac{\partial f_U(v, t)}{\partial v} \right]; \quad v \in (-\infty, +\infty), \quad (2.51)$$

where  $1/\tau > 0$  is the constant *mean reversion rate*. Applying equation (2.36a), the stationary distribution can be computed to be

$$f_{U_{\text{eq}}} = \frac{1}{(2\pi D\tau)^{1/2}} \exp\left(-\frac{v^2}{2D\tau}\right). \quad (2.52)$$

With a substitution of variables, eq. (2.51) can be transformed into a simpler diffusion equation with no drift term, that can be integrated to yield

$$f_{U(t)}(x) = \left( \frac{1}{\pi(1 - e^{-2t/\tau})} \right)^{1/2} \exp\left(-\frac{(x - x_0 e^{-t/\tau})^2}{1 - e^{-2t/\tau}}\right), \quad (2.53)$$

in terms of the reduced speed  $x = \sqrt{v^2/2D\tau}$  and the initial condition  $x_0$ .

Eq. (2.51) can also be obtained as an expansion in Hermite polynomials  $H_n$ . Using the reduced speed  $x$ , the explicit eigenvalues equation for the operator  $G_U$  (2.46) is

$$-\psi_n''(x) + x^2 \psi_n(x) = (\tau \lambda_n + 1) \psi_n(x). \quad (2.54)$$

This is the Schrödinger equation for a harmonic oscillator, and the solution is given in terms of the Hermite polynomials as  $\psi_n = e^{-x^2/2} H_n$ , with  $\tau \lambda_n = 2n$ . Then, the eigenfunctions of the FPO are  $\phi_n = e^{-x^2} H_n$ , and the general time-dependent solution is

$$f_{U(t)}(x) = e^{-x^2} \sum_{n=0}^{\infty} c_n H_n(x) e^{-2nt/\tau}, \quad (2.55)$$

where  $c_n$  are the expansion coefficients determined by the initial condition.



# Chapter 3

## Relativistic heavy-ion collisions as a diffusion process

This chapter discusses the application of the stochastic dynamics formalism previously presented to the case of relativistic heavy-ion collisions and the spectral method employed for the solution of the resulting FPE.

### 3.1 Relativistic diffusion

To successfully describe a relativistic process like heavy-ion collisions at LHC, with particles traveling close to the speed of light, a basic requirement is that the corresponding diffusion model is compatible with special relativity. That is not a trivial concern: as can be easily seen, Brownian motion and the original Ornstein-Uhlenbeck process, that describe the stochastic propagation of a particle, are inadequate to the scope. The normal distribution of velocities in equations (2.52) and (2.53) assigns a non-zero probability to per-luminal velocities, evidently clashing with special relativity.

Lopuszański [40], Dudley [41] and Hakim [42] have shown that stochastic process in position space cannot be both first-order Markovian and Lorentz-invariant. Since for practical purposes, one would like to maintain the convenience of the Markov property, at least a second-order process has to be used, as done in the Ornstein and Uhlenbeck treatment of Brownian motion. While, as discussed, in the original formulation no upper limit to velocities is enforced, this can be cured by basing the model on the particle's momentum  $\mathbf{p}$ , which remains unbounded in special relativity [13–15]. This leads to a  $(2d+2)$ -dimensional first-order Markov process in phase space  $(\mathbf{X}, \mathbf{P})$ , with<sup>1</sup>

$$dX^\mu(t) = \frac{P^\mu(t)}{P^0(t)} dt \quad \text{for } \mu = 0, \dots, d. \quad (3.1)$$

---

<sup>1</sup>Greek indices run from 0 to  $d$ , while Latin letters indicate only the spatial components. The Minkowski metric with signature  $(+, -, \dots, -)$  is adopted. Natural units are used:  $c = \hbar = k_B = 1$ .

In addition,  $\mathbf{P}$  obeys a SDE of the form eq. (2.26a), with the assumption that its coefficient functions do not explicitly depend on  $\mathbf{X}$ . Hence,  $\mathbf{P}$  can be treated as an independent drift-diffusion subprocess of  $(\mathbf{X}, \mathbf{P})$ , and  $\mathbf{X}$  is then completely determined by its relation (3.1) to the momentum. This does not imply that the system is homogeneous in position space, as that would require the initial state to be position-independent as well. The on-shell mass condition fixes

$$P^0(t) := \sqrt{m^2 + \sum_{i=1}^d (P^i(t))^2}, \quad (3.2)$$

where  $m$  is the particle mass, reducing the problem to  $2d$  degrees of freedom<sup>2</sup>. The choice of a time parameter  $t$  for the stochastic process singles out a preferred class of temporal hypersurfaces in Minkowskian space, which implicitly enters into the definition of the member PDFs  $f_{(\mathbf{X}, \mathbf{P})}(t)$  [43]. Here, the quantity  $f_{(\mathbf{X}, \mathbf{P})}(\mathbf{x}, \mathbf{p}, t) d^3x d^3p$  is the probability that the Brownian particle is located at some position  $\mathbf{x} \in [\mathbf{x}, \mathbf{x} + d\mathbf{x}]$  with momentum  $\mathbf{p} \in [\mathbf{p}, \mathbf{p} + d\mathbf{p}]$  at some time  $t$ . Writing equations (3.1) and (3.2), with

$$X^0(t) := t + \text{constant}, \quad (3.3)$$

these hypersurfaces are isochronous hyperplanes, which means that observables containing  $f_{(\mathbf{X}, \mathbf{P})}(t)$  are inherently non-local since they may contain information from space-like separated events. This should provide an appropriate comparison to data that are recorded approximately simultaneously in spatially extended detectors.

## 3.2 System and observables

During a relativistic heavy-ion collision, two highly relativistic nuclei collide interpenetrating each other, giving rise to a complex cascade of interactions resulting in a shower of produced particles. Immediately after the initial contact, the nucleons of each ion are separated into two fragments: a group of "spectators", that continue to travel almost undisturbed along the beam axis, and a group of "participants", that interact with the opposing fragment. Due to the high density of particles, a hot fireball of partonic matter forms between the receding fragments [45], where partons are deconfined, in a phase of matter called Quark-Gluon Plasma (QGP). After a brief phase of strong dynamics, local thermal and chemical equilibrium is reached. The main characteristic of this phase, which can be described by relativistic fluid dynamics, is a rapid expansion both in the longitudinal and transverse directions and a consequent dilution and cool down of the fluid. Once a critical temperature

---

<sup>2</sup>For ease of notation,  $\mathbf{x}$  and  $\mathbf{p}$  will be used from here on to indicate only the spatial components of position and momentum.

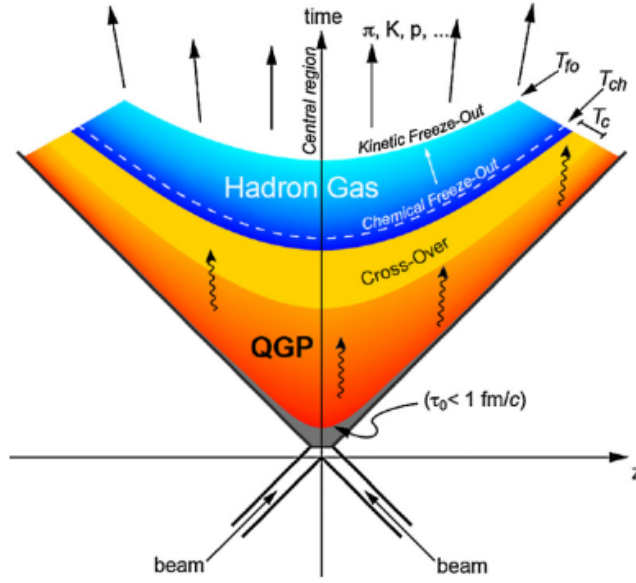


Figure 3.1: Space-time diagram of a heavy-ion collision of two nuclei colliding at time  $t = 0$  and longitudinal position  $z = 0$  (transverse direction not shown). For details see text. Figure from Ref. [44].

$T_C$  [46] has been reached, the fluid hadronizes in a parton–hadron crossover. When the temperature and density drop even further, up to a point where interactions are too scarce to maintain kinetic equilibrium, particles “free stream” towards the detector, in a process described as kinetic freeze-out. A schematic space-time diagram of a heavy-ion collision in the longitudinal direction is depicted in Fig. 3.1.

In this thesis only symmetric collisions in which the two nuclei are identical in terms of their numbers of protons  $Z$  and neutrons  $A - Z$  are considered. In this scenario, the most convenient coordinate system to describe the collision is the *center-of-momentum* (COM) frame, where the two ions move in opposite directions with the same absolute momentum. The total energy available in the collision, if every nucleon would participate in the interaction, is the total relativistic energy in the COM frame  $\sqrt{s}$ . The maximum energy per nucleon pair  $\sqrt{s_{NN}} = \sqrt{s}/A$  is also frequently used. The absolute relative longitudinal rapidity  $y_b$  between the two rest frames of the incoming nuclei is usually called the *beam rapidity*, and can be obtained from

$$y_b = \text{arcosh} \left( \frac{\sqrt{s_{NN}}}{2m_N} \right), \quad m_N \approx \frac{Zm_p + (A - Z)m_n}{A}, \quad (3.4)$$

where the average nucleon mass  $m_N$  is approximated as a weighted average of the proton mass  $m_p \approx 938.3$  MeV and neutron mass  $m_n \approx 939.6$  MeV, neglecting the binding energy of the nucleus.

Just before the collision, the state of the system is determined by the wave function of the incoming nuclei. However, the latter is a complicated object, not yet fully understood, and here the nuclei are approximated with idealized perfect spheres in their respective rest frames, neglecting any substructure due to individual nucleons or partons. In the COM frame, these spheres are Lorentz-contracted to oblate spheroids, loosely referred to as "pancakes", moving parallel to the *beam* or *longitudinal axis*. The plane perpendicular to it is referred to as the *transverse plane*, and projecting onto it the geometric centers of the nuclei yields two stationary points, whose distance is denoted as the *impact parameter*  $b$ . The origin of the Cartesian coordinates is placed at the geometric center of the system, and the third direction is oriented along the beam axis. The first and second axes span the transverse plane. Orienting then the first axis along the direction of  $b$ , it spans along with the longitudinal axis the *reaction plane*.

The focus of this thesis is limited to "central" collisions, in which the impact parameter  $b$  does not exceed 5% of the transverse size of the nuclei. Under this condition, the system possesses an approximate rotational symmetry around the longitudinal axis, that can be exploited by utilizing cylindrical coordinates  $(p_\perp, \phi, p^3)$

$$p_\perp := \sqrt{(p^1)^2 + (p^2)^2}, \quad \phi := \arg(p^1 + ip^2), \quad (3.5)$$

with  $p_\perp$  being the *transverse momentum*. Any physical observable expressed in the new set of coordinates, such as the stochastic trajectory of a particle, should then be in good approximation independent of the angle  $\phi$ . That implies that the stochastic process  $\mathbf{P}$ , after being expressed in cylindrical coordinates with the appropriate rules of stochastic calculus, can be reduced to a subprocess  $(P_\perp, P^3)$  whose drift and diffusion coefficients are independent of the redundant stochastic variable  $\Phi$ .

In addition, it is useful to transform the remaining momenta into hyperbolic rapidities. Firstly,  $p^3$  is replaced by the *longitudinal rapidity*  $y$

$$y := \operatorname{artanh} \left( \frac{p^3}{p^0} \right), \quad (3.6a)$$

$$\frac{\partial (p_\perp, p^3)}{\partial (p_\perp, y)} = \begin{pmatrix} 1 & 0 \\ \frac{\sinh(y)}{\sqrt{1+(m/p_\perp)^2}} & \sqrt{m^2 + p_\perp^2} \cosh(y) \end{pmatrix}. \quad (3.6b)$$

This coordinate is particularly convenient for Lorentz transformations along the beam axis since the particle trajectory expressed in  $(P_\perp, Y)$  can be boosted longitudinally by simply adding the relative boost rapidity  $\Delta y$  to  $Y(t)$  from the argument of the PDF,

$$f_{(P_\perp, Y)(t)+(0, \Delta y)}(p_\perp, y) = f_{(P_\perp, Y)(t)}(p_\perp, y - \Delta y). \quad (3.7)$$

Lastly,  $p_\perp$  is replaced by the *transverse rapidity*  $h$

$$h := \operatorname{arsinh} \left( \frac{p_\perp}{m} \right), \quad (3.8a)$$

$$\frac{\partial(p_\perp, y)}{\partial(h, y)} = \begin{pmatrix} m \cosh(h) & 0 \\ 0 & 1 \end{pmatrix}, \quad (3.8b)$$

which maps low and high transverse momenta into a linear and logarithmic scale.

### 3.3 Drift-diffusion model

As a final result of the collision, a shower of particles is measured by the surrounding detectors. After an accurate analysis of numerous events, the distribution of different particle species in phase space can be reconstructed. This information is encoded in the corresponding *number density functions* (NDFs), denoted by  $d^n N/d^n q$ , where  $\mathbf{q}$  is the relevant coordinate space, e.g.  $(y, p_\perp)$ . The total number of particles  $N$  is obtained by integrating  $d^n N/d^n q$  over the entire coordinate space. The connection to the PDFs of a stochastic diffusion model is simply made by scaling the latter by the total particle number

$$\frac{d^n N}{d^n q}(\mathbf{q}) = N f_{\mathbf{Q}}(\mathbf{q}, t^*), \quad (3.9)$$

where the stochastic process  $\mathbf{Q}$  describes the trajectory of the particle of interest in  $\mathbf{q}$ -space that hit the detectors at some time  $t^*$ .

The coefficient functions for the FPE of the process  $\mathbf{Q}$  are obtained via the FDR from an expected asymptotic state. However, eq. (2.39) only fixes the relation between the drift and diffusion coefficients, so another condition has to be set. For the moment, it will be assumed that the diffusion matrix for a process  $\Xi = (H, Y)$  in transverse and longitudinal rapidity,  $\xi = (h, y)$ , is diagonal and constant

$$D_\Xi = \begin{pmatrix} D_\perp & 0 \\ 0 & D_\parallel \end{pmatrix}. \quad (3.10)$$

With this simplification, the drift coefficient can be completely determined from the asymptotic state with the FDR (2.41). This approach is in line with those used in the previous, one-dimensional iterations of the model. In Chapter 4, a rapidity-dependent diffusion will be motivated and introduced, without deep consequences on the following consideration.

Under this ansatz, the FPE (2.33a) for the process  $\Xi$  assumes a particularly simple diagonal form

$$\frac{\partial}{\partial t} f_\Xi(t) = [L_\Xi^1 + L_\Xi^2] f_\Xi(t), \quad (3.11a)$$

with  $L_{\Xi}^i$  containing only derivatives with respect to the coordinate  $\xi^i$

$$L_{\Xi}^1(\xi) = D_{\perp} \frac{\partial}{\partial h} \left[ -\frac{\partial \ln f_{\Xi_{\text{eq}}}(\xi)}{\partial h} + \frac{\partial}{\partial h} \right], \quad (3.11b)$$

$$L_{\Xi}^2(\xi) = D_{\parallel} \frac{\partial}{\partial y} \left[ -\frac{\partial \ln f_{\Xi_{\text{eq}}}(\xi)}{\partial y} + \frac{\partial}{\partial y} \right]. \quad (3.11c)$$

### 3.3.1 Dimensionless formulation

Since rapidities are physically dimensionless, the only dimensionful quantities remaining in the associated FPE are the time parameter  $t$  and the diffusivity, having a dimension of time and inverse time, respectively. To eliminate these, the FPE can be rewritten in terms of a new, dimensionless evolution parameter  $\delta$  via  $t =: t_0 + \Delta t \delta$

$$\frac{\partial}{\partial \delta} f_{\Xi}(t_0 + \Delta t \delta) = \Delta t L_{\Xi} f_{\Xi}(t_0 + \Delta t \delta), \quad \delta > 0, \quad (3.12)$$

with the interaction timespan  $\Delta t := t^* - t_0$ . Here  $t_0$  represents the initial time, and solving the equation up to  $\delta = 1$  corresponds to evolving it until the final time  $t^*$ . Due to the shape of the FPO, the diffusivity coefficients and interaction timespan can be combined to form the dimensionless products  $D_{\perp} \Delta t$  and  $D_{\parallel} \Delta t$ , whose numerical values determine how close the final state is to the initial ( $D_{\perp} \Delta t, D_{\parallel} \Delta t \ll 1$ ) or asymptotic state ( $D_{\perp} \Delta t, D_{\parallel} \Delta t \gg 1$ ). This incidentally exposes an intrinsic symmetry of diffusive systems: changing the interaction timespan while reciprocally adjusting drift and diffusivity leaves the final state unchanged. Mathematically, this is related to a certain self-similarity of the standard Wiener process  $W(t)$ : for any constant  $\alpha > 0$ , the process  $\widetilde{W}(t) := \frac{1}{\sqrt{\alpha}} W(\alpha t)$  is also a standard Wiener process.

### 3.3.2 Multiple-sources ansatz

It is well known that in relativistic heavy-ion collisions energy and particle number densities are highly inhomogeneous in position space, so it can be expected that particle dynamics differ in space as well. This is not covered by the ansatz used in this thesis for the subprocess in momentum space  $\mathbf{P}$ , which assumes that its coefficient functions do not depend on any positional coordinates. To address this issue at least partly, in previous applications of the model, the ansatz (3.9) was generalized by splitting the system into multiple disconnected subsystems (“sources”) [47]

$$\frac{d^n N}{d^n q}(\mathbf{q}) = \sum_a N_a f_{\mathbf{Q}_a}(\mathbf{q}, t^*), \quad \text{with} \quad \sum_a N_a = N, \quad (3.13)$$

for which different initial and asymptotic states can be chosen, thereby decoupling their time evolutions with independent FPOs  $L_{\mathbf{Q}_a}$ . Conceptually, each source can be thought to occupy a distinct region in phase space, with overlap between



the different regions deemed negligible. Although this approach has been proven successful, its implementation has revealed itself particularly challenging for the solution method based on the spectral eigenfunction decomposition of the FPO. The reasons for that are discussed in detail in the next chapter, along with the nature and relative contribution of each source to particle thermalization at LHC energies, and in the rest of this thesis only a single source is considered, with meaningful results obtained nonetheless.

## 3.4 Charged-hadron thermalization

Due to the large number of particles present in the final stages of a relativistic heavy-ion collision, it is to be expected that mutual interactions lead to an ongoing thermalization of the system. However, the rapid expansion, particularly in the longitudinal direction, imposes a limitation on the interaction time, that arises both from the finite period until the hadrons reach the detectors and the dilution of the system due to its expansion, ultimately leading to a kinetic freeze-out. Consequently, it is expected [47] that the system never attains thermal equilibrium but rather persists in a transient state at the time of measurement.

These circumstances provide favorable conditions for employing non-equilibrium statistical models, with a specific emphasis on drift-diffusion processes. The abundance of particles and interactions implies that correlations are likely to be negligible so that the impact of particle-hadron collisions can be effectively represented by a stochastic force acting on the hadrons. Concurrently, the collective expansion of the system and frictional interactions with the surroundings are expected to introduce an additional deterministic component to the motion of the hadrons, which a suitable drift coefficient can appropriately address.

Indeed, promising results could already be obtained by Wolschin [18, 48] and Biyajima *et al.* [19] with a simple one-dimensional Ornstein–Uhlenbeck ansatz, which was later refined through the use of a non-linear drift term based on a thermal FDR [49]. Here, the latest three-dimensional version of the diffusion model by Hoelck & Wolschin [24] is solved with a spectral eigenfunction decomposition, overcoming the numerical accuracy limitation of the latter that restricted the authors to obtain predictions beyond the low transverse momentum region ( $p_{\perp} < 2$  GeV).

### 3.4.1 Initial state

The thermalization process is modeled to begin directly after the production of particles from hadronic interactions of the colliding nuclei, and the time evolution of the system is set to start from this initial time  $t_0$ . The resulting trajectories

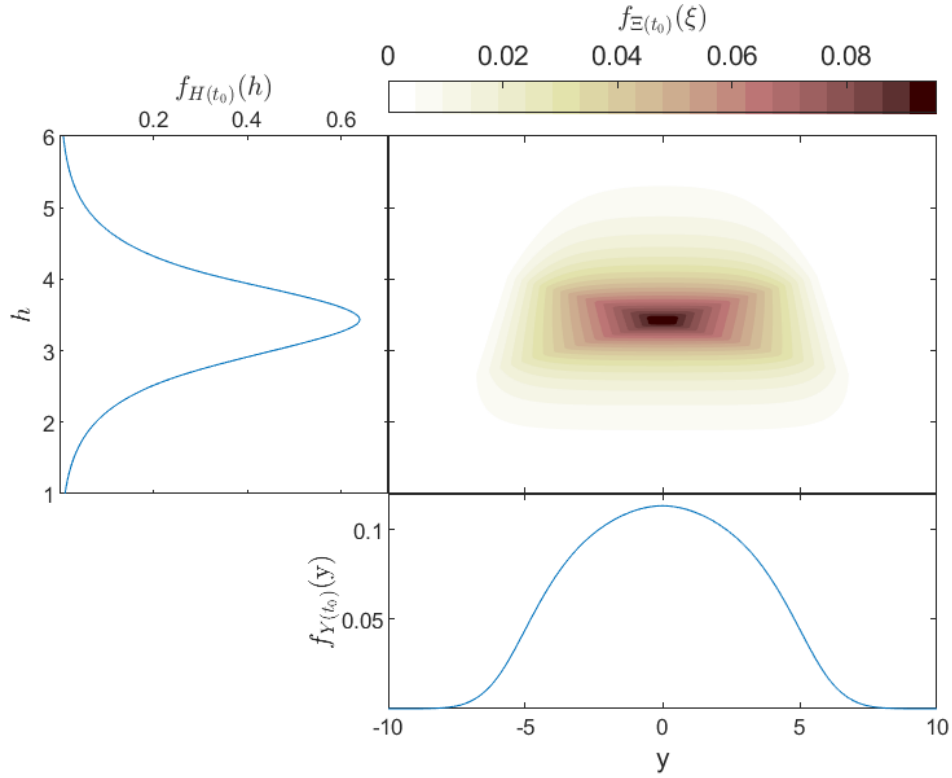


Figure 3.2: Initial PDF of the central gluon-gluon pions source, eq. (3.16a), for a  $\sqrt{s_{\text{NN}}} = 2.76$  TeV Pb-Pb collision. The joint distribution is shown in the central panel as a contour plot, with the color scale on the top. The left and the bottom panels contain the marginal PDFs in transverse and longitudinal rapidity, respectively.

are therefore to be interpreted in terms of *parton-hadron duality* since many of the produced particles immediately dissolve into their partonic constituents, which only later reassemble into real hadrons. The associated initial PDF are derived from a QCD-inspired phenomenological framework based on gluon saturation in the *deep-inelastic scattering* (DIS) of participant partons [50–53], that was already successfully used by Hoelck & Wolschin [23] in the context of baryon stopping, and which appears to be compatible with a recent analysis of initial-state signals in ALICE data [54].

The key assumption of this framework is that the gluon density saturates below a characteristic momentum scale  $Q_s$ , so that the respective gluons form a *color-glass condensate* (CGC). For small values of the gluon Bjorken momentum fraction  $x$ , this scale can be parametrized as [55]

$$Q_s^2(x) = \sqrt[3]{A} Q_0^2 \left( \frac{x_0}{x} \right)^\lambda, \quad (3.14)$$

where the values  $\lambda = 0.2$  and  $\frac{4}{9}Q_0^2x_0^\lambda = 0.09 \text{ GeV}^2$  are used to be consistent with Refs. [23, 24]. These values can be compared with literature results, where  $\lambda \approx 0.288$  and  $Q_0^2x_0^\lambda \approx 0.097 \text{ GeV}^2$  were determined in a fit to deep-inelastic scattering e-p data from HERA [55].

The interaction of the participating nucleons is assumed to be mediated by quark-antiquark pairs (“dipoles”) emitted by the confined partons, which then inelastically scatter off the partons of the oppositely moving nucleus. Subsequent recombination of the involved quarks and gluons results in the production of new hadrons, which are emitted from the nuclear fragments. From the mass  $m$  and rapidities  $(h, y)$  of the produced hadron, the Bjorken momentum fractions  $x_\pm$  of the two generating partons contained in the forward (+) and backward (−) moving nucleon can be reconstructed from kinetic considerations to be

$$x_\pm \approx \frac{m \cos(h) \exp(\pm y)}{2m_N \sinh(y_b)}, \quad (3.15)$$

with  $y_b$  and  $m_N$  as defined in eq. (3.4). Note however, that equation (3.15) is obtained by simply imposing energy and longitudinal momentum conservation, ignoring the initial transverse motion of the nucleons in the COM frame, as well as the comparatively small parton masses contribution to the energy and any additional valence quarks that may be needed, and is therefore an approximation.

At low Bjorken  $x$ , the nucleon momentum is mostly carried by gluons, while valence quarks prevail at high  $x$ . For two interacting partons, this results in four dominant interaction processes for the DIS that constitute the disconnected sources present in eq. (3.13): gluon-gluon (gg), gluon-valence quark (gq), valence quark-gluon (qg) and quark-quark (qq) interactions. As already anticipated, in this thesis, only one source is considered, the “central” gluon-gluon scattering which predominantly yields hadronic particle-antiparticle pairs with low to intermediate  $y$ . Their initial PDF can be approximated by [56]

$$f_{\Xi(t_0)}(\xi) \approx C_{\text{gg}} \sinh(h) \cosh(h) \prod_{i \in \{+, -\}} x_i \frac{G(x_i; m \sinh(h))}{\sinh(h)^2} \Theta(1 - x_i), \quad (3.16a)$$

where  $G$  is the simplified gluon structure function

$$xG(x; Q) \propto (1 - x)^4 \min(Q^2, Q_s^2(x)), \quad (3.16b)$$

and  $C_{\text{gg}}$  is a numerically determined normalization constant. Eq. (3.16a) is completely symmetric under the exchange of the forward- and backward-going gluon, and depends on the rapidity  $y$  through  $x_\pm(y, h)$ . The Heaviside theta functions are needed to ensure the validity of the Bjorken momentum fraction of the gluons since eq. (3.15) has physical sense only for  $x \leq 1$ . An illustration of eq. (3.16a) for a Pb-Pb collision at  $\sqrt{s_{\text{NN}}} = 2.76 \text{ TeV}$  is showed in Fig. (3.2).

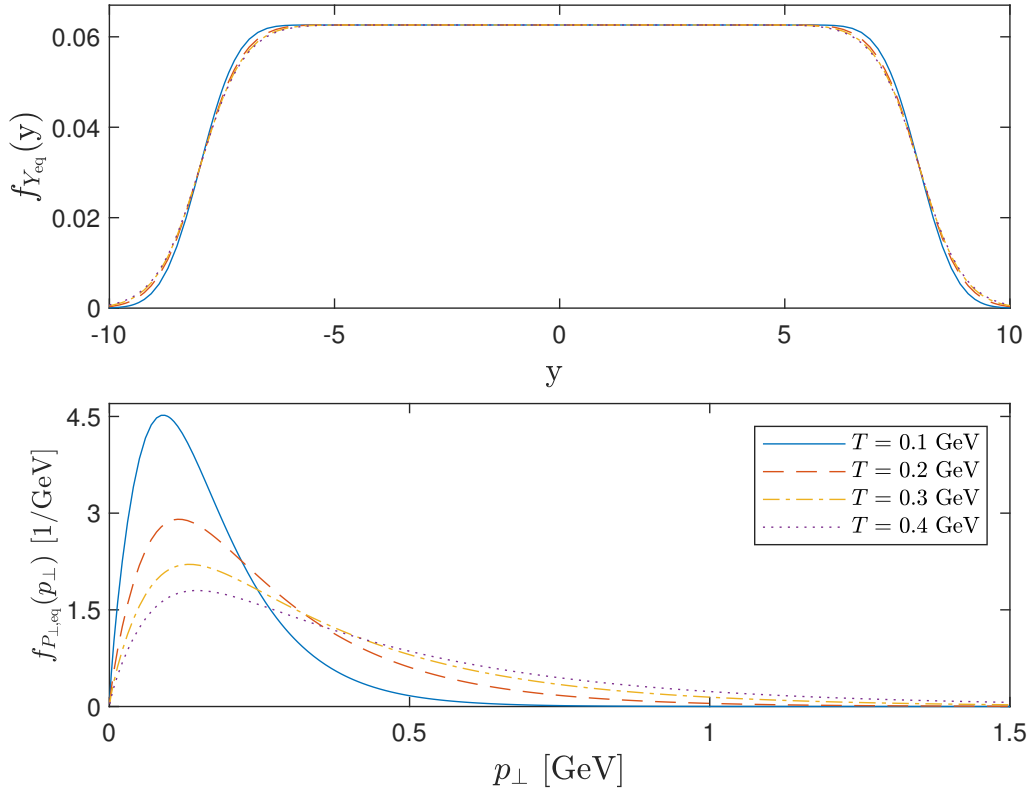


Figure 3.3: Asymptotic marginal PDFs for pions production in a  $\sqrt{s_{\text{NN}}} = 2.76$  TeV Pb-Pb collision for different temperatures  $T$ . Other parameters as in Table (4.1). Considering another particle species has the same effect as changing  $T$  for  $f_{Y_{\text{eq}}}$ , while greater masses move the peak of  $f_{P_{\perp, \text{eq}}}$  at higher  $p_{\perp}$ .

The hadron yield of the qq process is expected to be small compared to the other three and can thus be safely neglected, but one should not in principle ignore the contribution given by the interactions of gluons and valence quarks. These two "fragmentation" sources produce particles at higher rapidities than the central source, and while essential to describe baryon stopping, their relevance in particle thermalization for central collisions at LHC energies can be disregarded without heavy consequences. However, the reason why these sources are not included is simply the difficulty of accounting for their time evolution with the employed spectral eigenfunction decomposition, as illustrated in detail in section 4.1.

### 3.4.2 Asymptotic state

If the particles produced in a relativistic heavy-ion collision maintained their interactions for an extended period without ceasing due to the physical freeze-out, it is expected that the system would undergo thermalization and reach a stationary state in momentum space. In contrast, in position space, due to the absence of spatial confinement, the system cannot reach a stationary state that is independent of its

initial configuration, and it would continue to expand into the surrounding vacuum leading to a finite collective particle flow [57]. Consequently, the equilibrium state in momentum space of any produced charged hadron can be modeled by a generalized Maxwell-Jüttner distribution for an expanding thermal reservoir

$$f_{\mathbf{P}_{\text{th}}}(\mathbf{p}) := \frac{C_{\text{th}}}{V} \int_{\Sigma} \frac{d\sigma_{\mu} p^{\mu}}{p^0} \exp\left(\frac{m - u_{\nu} p^{\nu}}{T}\right), \quad (3.17)$$

where  $\Sigma \subseteq \mathbb{R}^{1,3}$  denotes the (3+1)-dimensional space-time hypersurface containing the reservoir and  $u_{\nu}$  its proper collective-flow velocity, which may depend on the position  $\sigma \in \Sigma$ . The total volume of the expanding reservoir is defined as  $V := \int_{\Sigma} d\sigma_{\mu} u^{\mu}$ , and  $C_{\text{th}}$  is a normalization constant independent of  $\Sigma$  and  $u_{\nu}$  that can be computed analytically to be

$$C_{\text{th}} = \frac{\kappa}{4\pi m^3 \exp(\kappa) K_2(\kappa)}, \quad (3.18)$$

in terms of the dimensionless ratio between mass and temperature  $\kappa := m/T$  and the modified Bessel function  $K_a$  of the second type and order  $a$ .

The simplest concrete implementation of (3.17) is obtained by considering a non-expanding reservoir at rest, i.e.  $u_{\nu} = 0$ , that leads to the original Maxwell-Jüttner distribution

$$f_{\mathbf{P}_{\text{MJ}}}(\mathbf{p}) = C_{\text{th}} \exp\left(\frac{m - p^0}{T}\right), \quad (3.19a)$$

which is the relativistic generalization of the Maxwell-Boltzmann distribution proposed by Jüttner [58] in 1911. It is useful to look at the marginal PDFs of (3.19a) in transverse and longitudinal rapidity space:

$$f_{H_{\text{MJ}}}(h) = \frac{\kappa}{K_2(\kappa)} \sinh(h) \cosh(h)^2 K_1(\kappa \cosh(h)), \quad (3.19b)$$

$$f_{Y_{\text{MJ}}}(y) = \frac{1}{2K_2(\kappa)} \left[ 1 + \frac{2}{\kappa \cosh(y)} + \frac{2}{(\kappa \cosh(y))^2} \right] \exp(-\kappa \cosh(y)). \quad (3.19c)$$

The *full width at half maximum* (FWHM) of the marginal rapidity distribution  $\Delta Y_{\text{MJ}}$  is bounded from above by its value at the infinite temperature limit of  $2 \operatorname{arcosh}(\sqrt{2})$  for every finite  $T$ . This fact, which holds for a purely spherical flow as well, is in contrast with experimentally observed charged-hadron distributions at LHC, that present a broader spectrum.

The authors of the reference model [24] have addressed this problem by considering a cylindrical-shaped expansion that spreads faster in the longitudinal than in the transverse direction. In detail, this is a Bjorken flow [45] in the longitudinal direction with maximum flow rapidity  $y_s$  [59]

$$f_{\Xi_{\text{Bj}}}(\xi) = \frac{1}{2y_s} \int_{-y_s}^{y_s} f_{\Xi_{\perp}}(h, y - \zeta) d\zeta \quad (3.20)$$

on top of a purely transverse expansion  $f_{\Xi_{\perp}}$ , the details of which are not here reported for conciseness. To account for the well-known fact that conventional

thermal models fail to describe the transverse high-momentum tails of charged-hadron data [60, 61], following a phenomenological model proposed by Hagedorn [61], the aforementioned authors replaced the exponential in eq. (3.17) by

$$\widetilde{\text{exp}}(x; n) := \left(1 + \frac{x}{n}\right)^n, \quad \text{with} \quad x = \frac{m - u_\nu p^\nu}{T}. \quad (3.21)$$

For small values of its argument, that is for  $|x/n| \ll 1$ , eq. (3.21) behaves as an exponential function:  $\widetilde{\text{exp}} \sim \exp(x)$ ; On the other hand, for  $|x/n| \gg 1$ , it scales as a power law:  $\widetilde{\text{exp}} \sim (x/n)^n$ . This behavior should be able to capture the observed transition from a thermal distribution at low transverse momentum to a power-law decay (Pareto law) in the  $p_\perp$  tail of charged-hadron spectra, which is often attributed to the increasing importance of “hard” processes in this regime, which are not covered by thermal physics. However, when comparing to experimental data with  $p_\perp > 2$  GeV, it became clear that the value of  $n = -8$ , adopted in [24] following an analysis of ALICE p-p data [62], overestimates the particle yield at high- $p_\perp$ . Different values of  $n$  improve the situation in the momentum tail, but only at the expense of a decreased accuracy in describing the low- $p_\perp$  region.

Zheng *et al.* [63] have successfully employed a *generalized Fokker-Plank solution* (GFPS) to describe charged particle transverse distributions at different LHC energies and centralities:

$$f_{E_\perp \text{GFPS}}(E_\perp) = C_{\text{GFPS}} \left[ 1 + \left( \frac{E_\perp}{b} \right)^d \right]^{-c} \exp \left( -\frac{b}{T} \arctan \frac{E_\perp}{b} \right), \quad (3.22)$$

where  $E_\perp := \sqrt{p_\perp^2 + m^2} - m$ . When  $p_\perp \ll 1$  or  $\frac{E_\perp}{T} \ll 1$ ,  $f_{\text{GFPS}}$  behaves as  $e^{-E_\perp/T}$ , while in the high-momentum limit it follows the power law  $p_\perp^{-cd}$ . Motivated by the success of eq. (3.22) in describing the transverse spectra across multiple orders of magnitude, in this thesis the asymptotic distribution of the central gluon-gluon source is modeled as

$$f_{\Xi_{\text{eq}}}(\xi) = f_{H_{\text{GFPS}}}(h) \frac{1}{2y_s} \int_{-y_s}^{y_s} f_{Y_{\text{MJ}}}(y - \zeta) d\zeta, \quad (3.23)$$

which is the product of eq. (3.22) expressed in terms of the transverse rapidity  $h$ , including the determinant of the transformation, and a Bjorken flow in  $y$  based on the marginal Maxwell-Jüttner distribution eq. (3.19c). When considering its marginal rapidity distribution,  $f_{Y_{\text{eq}}}(y)$  is only slightly different from  $f_{Y_{\text{Bj}}}(y)$  obtained by marginalizing eq. (3.20), but it describes better the transition from exponential to power-law decay in the transverse direction. In addition, the product form  $f_{\Xi_{\text{eq}}} = f_{H_{\text{eq}}} f_{Y_{\text{eq}}}$  greatly speeds up the numerical solution. While in general such a form may not describe precisely the expected two-dimensional asymptotic state in the whole phase-space, it is here proposed that this approximation is good enough for low-to-intermediate rapidity, where  $f_{Y_{\text{eq}}}$  is essentially constant. Since no

experimental data are available beyond this region, it is difficult to speculate where this statement starts to fail.

## 3.5 Spectral method of solution

Spectral methods represent a powerful and versatile class of numerical techniques employed to solve partial differential and integral equations. Unlike traditional finite difference or finite element methods, the idea at the foundations of spectral methods is expressing solutions in terms of basis functions with global support. When applied to a smooth problem with a simple domain, spectral methods can achieve exceptional accuracy compared to other numerical methods, and the convergence is usually exponential in the number of basis functions or evaluation points. Among the abundant literature treating this broad subject, of particular help for the scope of this thesis was the textbook by Shizgal [64], which covers in detail the application of spectral methods to kinetic theory and Fokker-Planck and Schrödinger problems, and the one by Trefethen [65], that gives an introduction about their implementation in MATLAB.

In this section, the use of non-classical orthogonal polynomials to efficiently construct a spectral representation of the FPO will be discussed. Using such a basis set, it is possible to implement a representation of the one-dimensional operator that does not require an explicit calculation of the drift coefficient via the FDR, while for the higher-dimensional case, the equivalence between the Fokker-Planck and a Schrödinger equation will be exploited.

To construct a non-classical basis set, consider the polynomials  $\{P_m\}$  orthonormal with respect to some weight function  $w$  on  $(a, b) \in \mathbb{R}$ , that is,

$$\int_a^b w(x) P_m(x) P_l(x) dx = \delta_{ml}. \quad (3.24)$$

The polynomials form a basis set and satisfy the general three-term recurrence relation [66]

$$x P_m(x) = \sqrt{\beta_m} P_{m-1}(x) + \alpha_m P_m(x) + \sqrt{\beta_{m+1}} P_{m+1}(x), \quad (3.25)$$

where the coefficients  $\alpha_m$  and  $\beta_m$  can be determined with the Stieltjes procedure developed by Gautschi [67]. In this thesis, the MATLAB adaptation `stieltjes.m` of a FORTRAN routine [68] by the aforementioned author is used to generate the recurrence coefficients of an arbitrary weight function.

### 3.5.1 Spectral representation of the 1- $d$ FPO

As seen in subsection 2.4.4, it is possible to bring the one-dimensional FPO into a Hermitean form by multiplying it by  $e^\Phi$ , that is, by dividing it by the stationary

solution  $f_{X_{\text{eq}}}$ <sup>3</sup>, but no explicit expression for this form was given. Writing the general time-dependent solution  $f_X(x, t)$  as the product of the stationary solution and an auxiliary function  $g_X(x, t)$

$$f_X(x, t) := f_{X_{\text{eq}}}(x)g_X(x, t), \quad (3.26)$$

the FPE for the function  $g_X$  becomes

$$\begin{aligned} \frac{\partial g_X}{\partial t} &= \frac{1}{f_{X_{\text{eq}}}} \frac{\partial}{\partial x} \left[ D_X f_{X_{\text{eq}}} \frac{\partial g_X}{\partial x} \right] \\ &= \mu_X \frac{\partial g_X}{\partial x} + D_X \frac{\partial^2 g_X}{\partial x^2} = G_X g_X, \end{aligned} \quad (3.27)$$

where  $G_X$  is self-adjoint with respect to the equilibrium solution as a weight function<sup>4</sup>

$$\begin{aligned} \langle \phi_1 | G_X | \phi_2 \rangle &= \int f_{X_{\text{eq}}} \phi_1 G_X \phi_2 dx \\ &= \int f_{X_{\text{eq}}} \phi_2 G_X \phi_1 dx = \langle \phi_2 | G_X | \phi_1 \rangle, \end{aligned} \quad (3.28)$$

provided the zero flux boundaries condition

$$\int_{\partial V} f_{X_{\text{eq}}} D_X \frac{\partial g}{\partial x} dx = 0. \quad (3.29)$$

To construct an efficient spectral representation of the operator  $G_X$ , a basis of non-classical polynomials  $\{P_m\}$  orthogonal w.r.t. the stationary solution of the FPE can be employed. Such a basis satisfies eq. (3.24) with  $w = f_{X_{\text{eq}}}$ , and has the advantage that is automatically adapted to the specific problem. In addition, knowing that the first eigenfunction of the FPO is the equilibrium distribution and that the successive eigenfunctions are orthogonal to it, a basis set satisfying the same orthogonality relations is intuitively "special" compared to other polynomial sets. The spectral representation of  $G_X$  in this basis is [69–71]

$$\begin{aligned} G_X^{\text{ml}} &= \int f_{X_{\text{eq}}} P_m G_X P_l dx \\ &= \int f_{X_{\text{eq}}} P_m \frac{1}{f_{X_{\text{eq}}}} \frac{d}{dx} \left[ f_{X_{\text{eq}}} D_X \frac{dP_l}{dx} \right] dx. \end{aligned} \quad (3.30)$$

Integrating by parts and making use of the orthogonality of the basis set w.r.t. the stationary solution, the expression simplifies to

$$G_X^{\text{ml}} = \int f_{X_{\text{eq}}} D_X P'_m P'_l dx, \quad (3.31)$$

<sup>3</sup> $f_{X_{\text{eq}}}$  is assumed to be normalized, such that all normalization factors are ignored in this section.

<sup>4</sup>With abuse of notation, in eq. (3.27) the same symbol as in eq. (2.46) is used, even though in that case the self-adjointness of  $G_X$  was defined w.r.t. the unit function, and the two are thus different operators.



where natural boundary conditions were assumed. The representation (3.31) is particularly convenient because it only requires polynomial derivatives that can be carried out analytically. Since the drift function does not explicitly appear in the expression, if one already knows the stationary solution and the form of the diffusion coefficient, as is the case in this thesis, the use of the FDR is not even necessary. The eigenvalues  $\lambda_m$  and eigenfunctions  $\psi_m$  of the operator  $G_X$  can be estimated by diagonalization of the  $(M + 1) \times (M + 1)$  symmetric matrix  $G_X^{\text{ml}}$ , where  $M + 1$  is the dimension of the orthonormal basis set  $\{P_m\}$ . It was shown numerically that the coefficients of the expansion of  $\psi_n$  in the  $\{P_m\}$  basis set are linear variational parameters. The variational theorem then guarantees that this method provides an upper bound to the eigenvalues for each  $M$  and converges from above.

The FPO and  $G_X$  share the same eigenvalues, and are connected through

$$G_X = e^\Phi L_X e^{-\Phi}. \quad (3.32)$$

The time-dependent solution of the FPE can be then approximated by

$$f_X(x, t) \approx f_{X_{\text{eq}}}(x) \sum_{m=0}^M c_m \psi_m(x) e^{-\lambda_m(t-t_0)}, \quad (3.33)$$

where the coefficients  $c_m$  are determined from the initial condition by

$$c_m = \int f_X(x, t_0) \psi_m(x) dx. \quad (3.34)$$

The goodness of expression (3.33) in approximating  $f_{X(t)}$  depends of course on the convergence of the eigenvalues and eigenfunctions of the FPO, and equally importantly on the convergence of the coefficients  $c_m$  to small values approaching the  $M$ -th element.

### 3.5.2 Representation of the 2- $d$ Schrödinger operator

The stochastic process eqs. (3.11a–c) is characterized by a two-dimensional FPO, for which the simple 1- $d$  representation described above cannot be employed. The equivalence between the FPE and a Schrödinger equation with a supersymmetric potential is a well-understood fact [33, 72], and it is useful to take advantage of the large availability of solution methods of quantum mechanical problems. Finding a spectral solution of the FPO can be then reduced to the eigenvalues equation of a 2- $d$  Hamiltonian

$$-\frac{1}{2} \nabla^2 \psi_{\text{nm}}(\mathbf{x}) + V(\mathbf{x}) \psi_{\text{nm}}(\mathbf{x}) = \lambda_{\text{nm}} \psi_{\text{nm}}(\mathbf{x}), \quad \mathbf{x} = (x, y), \quad (3.35)$$

where the Schrödinger potential  $V$  can be obtained from the drift and diffusion coefficient functions. An explicit transformation in the case of constant diagonal diffusion is given in Ref. [73].

Unfortunately, it is not generally possible to construct an orthonormal set of polynomials of two variables  $(x, y)$  w.r.t. some weight function  $w(x, y)$ . Instead, two different basis set  $\{G_n(x)\}$  and  $\{H_m(y)\}$  have to be constructed, orthogonal w.r.t. two weight functions  $u(x)$  and  $q(y)$ , respectively. The logarithmic derivatives of the weight functions are denoted by

$$U(x) := -\frac{u'(x)}{u(x)}, \quad Q(y) := -\frac{q'(y)}{q(y)}, \quad (3.36)$$

for ease of notation in the next equations. Making use of this two-dimensional basis set, the representation of the Schrödinger operator generating the eigenvalues equation (3.35) is [70]

$$H_{n'm',nm} = \delta_{m'm} \int u(x) G_{n'}'(x) G_n'(x) dx + \delta_{n'n} \int v(y) H_{m'}'(y) H_m'(y) dy + (V_{n'm',nm} - \tilde{V}_{n'm',nm}). \quad (3.37)$$

The potential matrix elements are  $V_{n'm',nm} = \langle X_{n'} Y_{m'} | V(x, y) | X_n Y_m \rangle$  and the matrix elements of the reference potential are

$$\begin{aligned} \tilde{V}_{n'm',nm} = & \delta_{m'm} \int \left( \frac{U^2(x)}{4} - \frac{U'(x)}{2} \right) u(x) G_{n'}'(x) G_n'(x) dx \\ & + \delta_{n'n} \int \left( \frac{Q^2(y)}{4} - \frac{Q'(y)}{2} \right) v(y) H_{m'}'(y) H_m'(y) dy. \end{aligned} \quad (3.38)$$

In contrast to the one-dimensional representation (3.31), the explicit calculation of the drift coefficient and its derivative is necessary to construct the potential  $V$ . If  $\mu_{\mathbf{X}}$  is constructed from the FDR, that means carrying out second derivatives of the asymptotic PDF.

# Chapter 4

## Results

The chapter is structured as follows: in the first section, the convergence of the spectral eigenfunction expansion in solving the FPE describing hadron thermalization in relativistic heavy-ion collisions is discussed. Then, before comparing to experimental data, some preliminary results are incorporated into the model, and the extension to a rapidity-dependent diffusion is motivated. In the third section, the model prediction are compared to experimental data from ALICE [25–27] and ATLAS [28] of  $^{208}\text{Pb-Pb}$  collisions with  $\sqrt{s_{\text{NN}}} = 2.76$  and 5.02 TeV. Lastly, a prediction is made for the spectra of the ongoing LHC run at  $\sqrt{s_{\text{NN}}} = 5.36$  TeV.

### 4.1 Convergence of the spectral expansion

For reasons that will be apparent in the next section, the discussion of the FPE spectral solution convergence is here limited to the marginal one-dimensional rapidity FPO

$$L_Y = D_{\parallel} \frac{\partial}{\partial y} \left[ -\frac{\partial \ln f_{Y_{\text{eq}}}(y)}{\partial y} + \frac{\partial}{\partial y} \right], \quad (4.1)$$

which can be solved employing the representation eq. (3.33) after the transformation to its Hermitean form  $G_Y$ . In Fig. 4.1, the extremely fast convergence of this solution scheme is shown when considering the FPO generated by the marginal rapidity central gluon-gluon source asymptotic PDF for hadron thermalization in a Pb-Pb collision at  $\sqrt{s_{\text{NN}}} = 2.76$  TeV with constant diffusion  $D_{\parallel}$ . As inferred from Fig. 4.1a), using an orthogonal basis of dimension  $M = 15$  is already sufficient to obtain a good convergence of the first five positive eigenvalues. Given this fact, for the subsequent results presented in this work, a basis dimension of  $M = 25$  is employed, which is deemed sufficient for obtaining a satisfactory precision of the relevant FPE solution. Panel b) shows on a logarithmic vertical scale the exponential approach to zero of the expansion coefficients  $c_m$ , calculated using eq. (3.34) with the initial PDF of the central gg source eq. (3.16a) and the eigenfunctions of  $G_Y$  calculated with  $M = 25$ . The values of the coefficients corresponding to odd eigenfunctions are zero up to

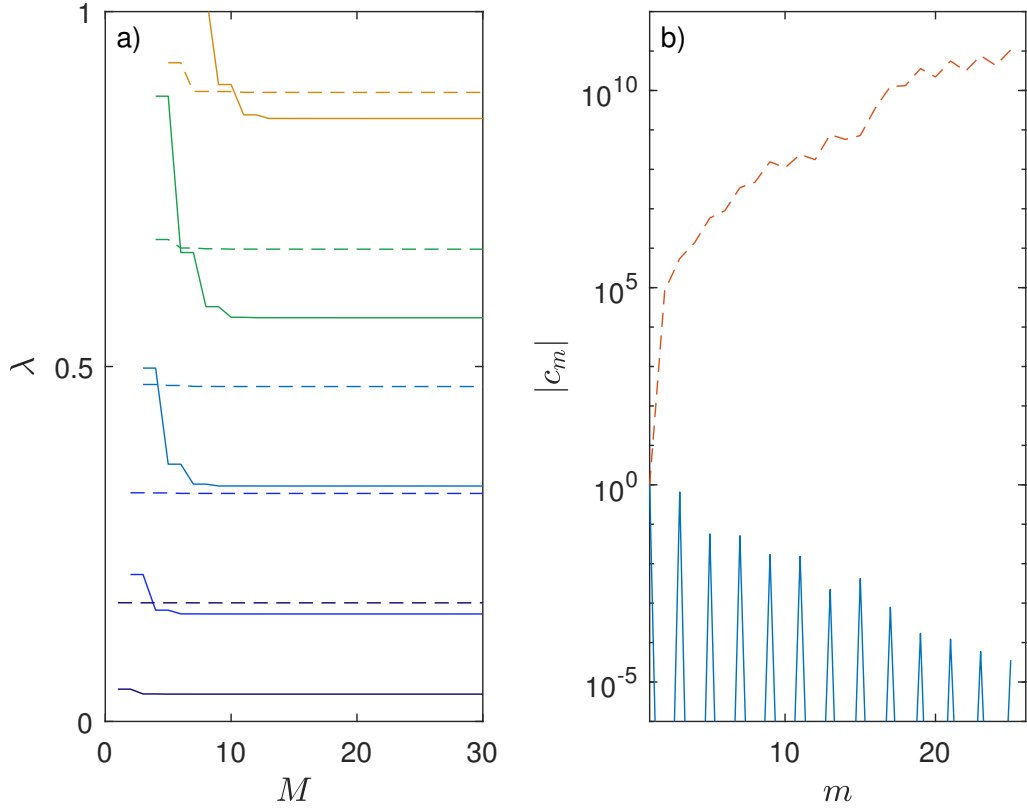


Figure 4.1: Spectral convergence of the FPE for the central gluon-gluon (solid curves) and the fragmentation sources (dashed curves). a) The first five positive eigenvalues of the adimensional marginal rapidity FPO are plotted against the orthogonal basis dimension  $M$ . The eigenvalues of the fragmentation FPO are scaled by 0.18 for better visualization. b) Absolute value of the expansion coefficients  $c_m$  (logarithmic scale) calculated from the initial PDF of the central (solid) and forward (dashed) sources.  $M = 25$ .

machine precision, as expected by the  $y$ -parity of both the FPO and the initial condition.

In contrast to the success of this spectral solution scheme in solving the central source FPE, Fig. 4.1 also illustrates its failure when applied to the forward quark-gluon and backward gluon-quark fragmentation sources. In panel a), the dashed lines show that the convergence of the eigenvalue is even faster than for the gg source, but from panel b) it can be observed that the absolute values of  $c_m$  explode for the higher eigenfunctions, and therefore a good approximation of the initial state with a finite-dimensional polynomial basis orthogonal to  $f_{Y_{\text{eq}}}$  cannot be reached. To understand why that is the case, the fragmentation equilibrium and initial states rapidity dependence have to be analyzed. Similarly to the central fireball, the marginal longitudinal asymptotic state is given by a  $y$ -symmetric Bjorken flow eq. (3.20) for both the gq and qg sources. The (backward)forward source initial PDF is again

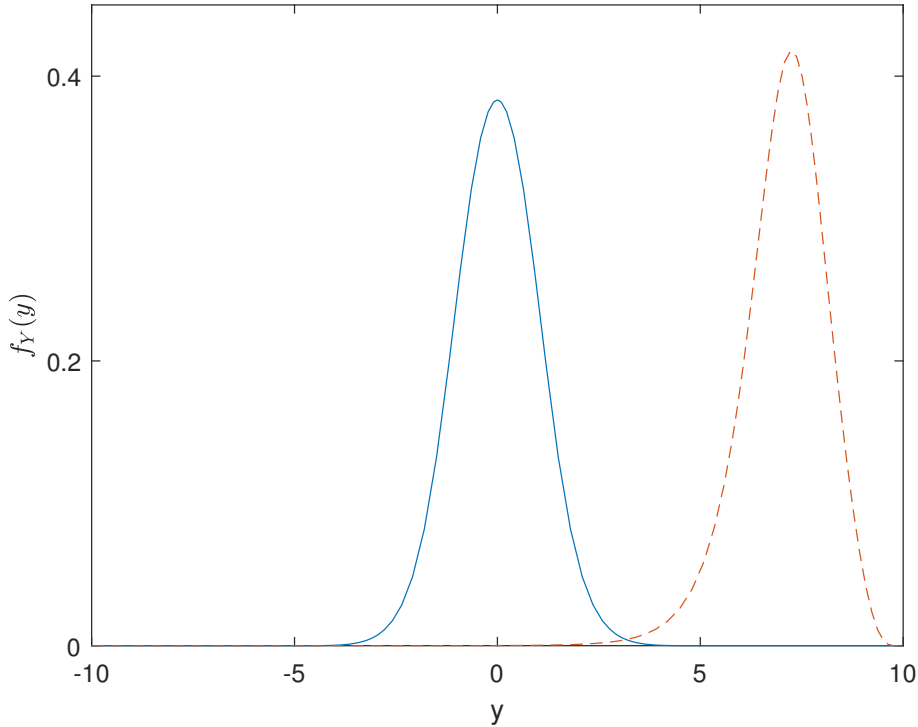


Figure 4.2: Initial (dashed) and equilibrium (solid) marginal rapidity PDF of the forward fragmentation source as described in [24].

derived from the DIS-CGC formalism, and is peaked around  $(-)y_b$ . Although their explicit expressions are not reported for conciseness, the forward qg marginal rapidity asymptotic and initial PDF, as employed in [24], are drawn in Fig. 4.2 for a  $\sqrt{s_{\text{NN}}} = 2.76$  TeV Pb-Pb collision. It is easy to see, that the two distributions occupy in practice two almost disconnected supports on the rapidity axis. At the peak of  $f_Y(t_0)$ , the extremely fast decay of  $f_{Y_{\text{eq}}}$  has already reached a machine noise level. While it is theoretically true that an infinite-dimensional orthogonal basis set defined by eq. (3.24) on  $\mathbb{R}$  is complete, and can then approximate any continuous function, in practice one can only generate a finite set. Following these considerations, it is not surprising that using  $f_{Y_{\text{eq}}}$  as a weight function to generate such a set determines a difficulty in approximating a function that peaks where the former is essentially zero.

## 4.2 Preliminary considerations

For  $^{208}\text{Pb}$ -Pb collisions at LHC, the only available data in the rapidity region up to  $y = 5$  are for unidentified electrically-charged hadrons ( $h^\pm$ ), because no suitable spectrometer for hadron identification has been installed yet. Consequently, the measured distributions are given in terms of the coordinates  $(p_\perp, \eta)$ , where  $\eta$  is the

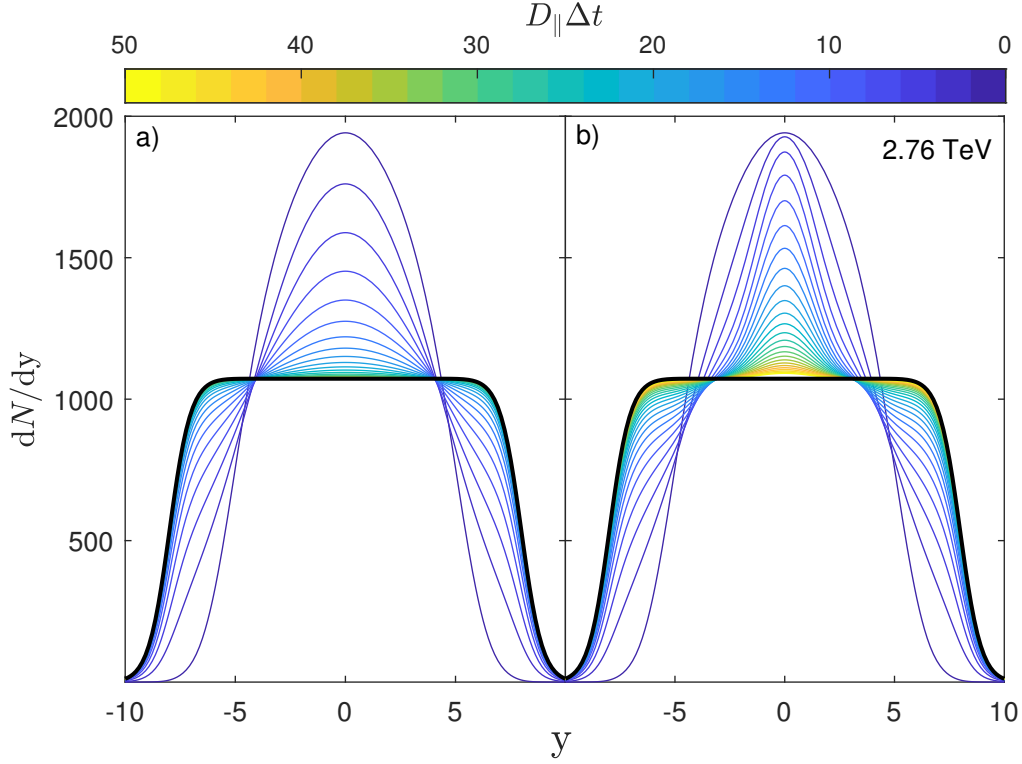


Figure 4.3: Time evolution of the marginal rapidity NDF for a  $\sqrt{s_{\text{NN}}} = 2.76$  TeV Pb-Pb collision, with parameters as in Table (4.1). The thick black lines indicate the asymptotic state, and the most narrow curves are calculated from the initial PDFs. Every line between the two extremes is separated by the one above by an increase in  $D_{\parallel}\Delta t$  of 2. a) Constant longitudinal diffusion,  $D_Y = D_{\parallel}$ ; b)  $D_Y = D_{\parallel}(1 - e^{-y^2/y_b})$ .

*pseudorapidity*

$$\eta := \text{artanh}\left(\frac{p^3}{|\mathbf{p}|}\right) = \text{arsinh}\left(\sqrt{1 + \left(\frac{m}{p_{\perp}}\right)^2} \sinh(y)\right), \quad (4.2a)$$

with the Jacobian

$$\frac{\partial(p_{\perp}, \eta)}{\partial(p_{\perp}, y)} = \begin{pmatrix} 1 & 0 \\ -\frac{\tanh(\eta)}{p_{\perp} \left[1 + \left(\frac{p_{\perp}}{m}\right)^2\right]} & \sqrt{1 + \left(\frac{m}{p_{\perp} \cosh(\eta)}\right)^2} \end{pmatrix}. \quad (4.2b)$$

The measurement of  $\eta$  only requires knowledge of the inclination angle of the particles trajectory to the beam axis, which is available even without particle identification, and  $\eta$  agrees with  $y$  for  $|\mathbf{p}| \gg m$ . The charged particle yield is mainly composed of pions, followed by kaons and (anti)protons, with the measured abundance fractions of approximately 83%, 13%, and 4%, respectively [74, 75].

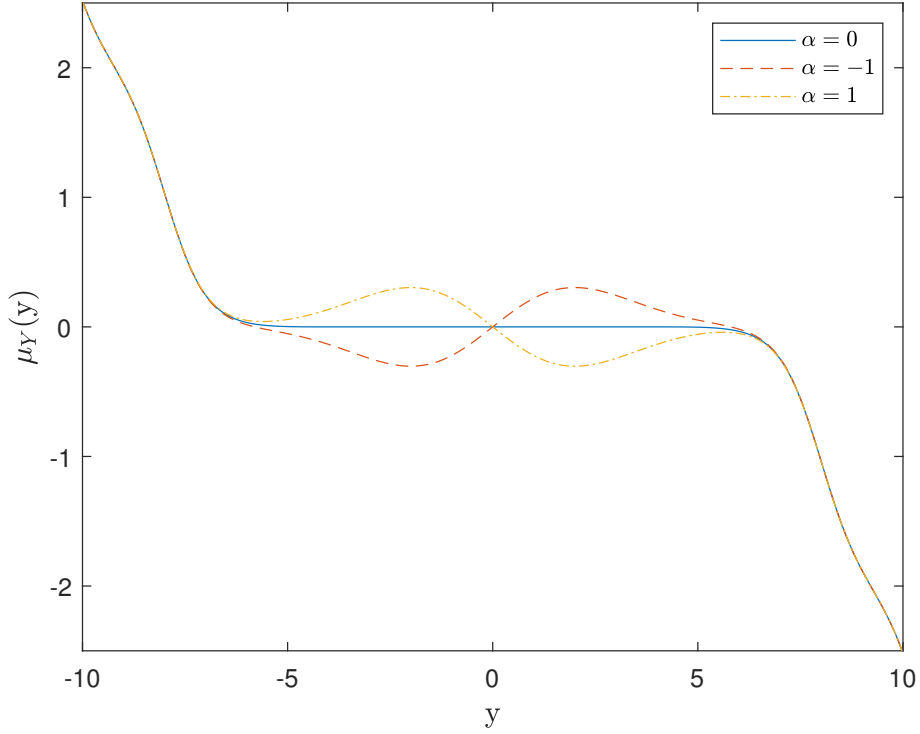


Figure 4.4: Drift coefficient  $\mu_Y$  of the marginal rapidity adimensional FPO for different values of  $\alpha$ . The  $f_{Y_{\text{eq}}}$  in the FDR describe pion thermalization in a  $\sqrt{s_{\text{NN}}} = 2.76$  TeV Pb-Pb collision. Parameters as in Tab. (4.1), except for  $D_{\parallel}\Delta t = 1$ . The solid blue line, corresponding to  $\alpha = 0$ , represents the case of a constant diffusion; The dashed red line and the dot-dashed yellow line are calculated for  $\alpha = -1$  and  $\alpha = 1$ , respectively.

Comparison with data from ALICE [25–27] and ATLAS [28] of Pb-Pb collisions with  $\sqrt{s_{\text{NN}}} = 2.76$  and 5.02 TeV is performed by evolving the initial PDF of the three hadron species separately with a common value of  $\mathbf{D}_{\Xi}\Delta t$  in the  $(h, y)$  coordinate space. Then, the obtained PDFs are transformed to the  $(p_{\perp}, \eta)$  space with the appropriate determinant, multiplied by the total number of particles  $N$ , and finally summed according to the above percentages. While in principle every particle species could have an independent set of parameters, the lack of identified hadron spectra would make the then abundant parameter space difficult to fit meaningfully to the available data. For this reason, the initial and final PDFs for pions, kaons, and protons are assumed to differ only by the respective particle masses, that are  $m_{\pi} = 139.6$  MeV,  $m_k = 493.7$  MeV, and  $m_p = 938.3$  MeV, and share the rest of the free parameters.

The parameter space can be additionally reduced by adopting two intermediate results obtained in the previous iteration of the model [24]. There, the maximum Bjorken flow rapidity  $y_s$  for the central gluon-gluon source was identified

with the beam rapidity  $y_b$ , and it was verified that the equilibration in the transverse direction happens much faster than in the longitudinal one, corresponding to  $D_\perp \Delta t \gg D_\parallel \Delta t$ . While this is not physically surprising, as thermal models with modified high-momentum tails are known to well describe the transverse charged-hadrons spectrum, it affects negatively the solution of the FPE. Following the same approach as in [24], the problem is circumvented by taking the limit  $D_\perp \Delta t \rightarrow \infty$ , which in practice means assuming an almost instantaneous thermalization in the transverse direction. Hence, the problem reduces to solving only the marginal one-dimensional longitudinal FPE

$$\frac{\partial f_Y}{\partial t} = \left[ -\frac{\partial}{\partial y} \mu_Y + \frac{\partial^2}{\partial y^2} D_Y \right] f_Y, \quad (4.3)$$

which can be done with the efficient spectral representation (3.31). The two-dimensional joint distribution can be then reconstructed by

$$\begin{aligned} f_\Xi(\xi, t^*) &\approx f_Y(y, t^*) f_{H_{\text{eq}}|Y_{\text{eq}}}(h|y) \\ &= \frac{f_Y(y, t^*)}{f_{Y_{\text{eq}}}(y)} f_{\Xi_{\text{eq}}}(\xi). \end{aligned} \quad (4.4)$$

Since the explicit use of the FDR is not necessary in this simplified case, and being motivated by the difficulty of a constant longitudinal diffusion coefficient to reproduce the midrapidity region encountered in the investigation above, it is straightforward to allow for a rapidity-dependent diffusion  $D_Y(y)$ . Imposing that  $D_Y$  is continuous, differentiable, positive for all  $y$  and respects the even symmetry of the system, a simple form is given by

$$D_Y(y) = D_\perp (1 + \alpha e^{-y^2/y_b}), \quad \alpha > -1, \quad (4.5)$$

where the denominator of the exponential is chosen to be  $y_b$  as it is the only fixed rapidity scale of the system, and treating it as a free parameter does not improve significantly the fit to the data. Since the solution obtained with a constant diffusion predicted a particle yield around  $y = 0$  too low compared to the data, and that in that region the PDF is monotonically decreasing in the time evolution, it is to be expected that negative values of  $\alpha$  should describe better the hadron spectra, as indicated by the fit to LHC data in the next section. Figure 4.3 shows the time evolution of the PDF for a  $\sqrt{s_{\text{NN}}} = 2.76$  TeV Pb-Pb collision for  $\alpha = 0$  and  $\alpha = -1$ . For constant diffusion, the approach to equilibrium is more uniform and significantly faster than in the second, such that the curves representing the latest times are indistinguishable from the equilibrium state. In the latter, it is clear that the equilibration is slower at  $y = 0$ , where  $D_Y$  vanishes, than at larger rapidities. For completeness, the drift coefficient  $\mu_Y$  is calculated via the FDR and showed for three different values of  $\alpha$  in Fig. 4.4.



$\sqrt{s_{\text{NN}}}$	$y_b$	$N \times 10^{-4}$	$D_{\parallel}\Delta t$	$\alpha$	$T/\text{MeV}$	$b \times \text{MeV}$	$cd$	$\chi^2/\text{ndf}$
2.76	7.99	1.713(8)	0.98(9)	-1	486(4)	9.4(5)	0.30(2)	134/193
5.02	8.58	2.182(8)	1.055*	-1	624(7)	22(4)	2.8(2)	28/66
5.36	8.65	2.237*	1.063*	-1*	639*	24*	3.06*	-

Table 4.1: Model’s free parameters determined by the  $\chi^2$  minimization to ALICE and ATLAS data, and extrapolation to  $\sqrt{s_{\text{NN}}} = 5.36$  TeV. Numbers in brackets indicate the estimated uncertainty of the preceding digit; see text for details. Numbers marked with \* are extrapolated as explained in the text. The value of  $c$  is fixed to 5.

### 4.3 Comparison with the experimental spectra

Allowing for a non constant diffusion, the free parameters of the model are  $D_{\parallel}\Delta t$  and  $\alpha$  that determine how and how much the solution approaches equilibration, the total number of particles  $N$ , and the parameters of the equilibrium PDF; those are the temperature  $T$ ,  $b$ , and the exponents  $c$  and  $d$ . The fit to experimental data is based on a least- $\chi^2$  determination. For every data point, the calculated PDF is integrated in the respective coordinate bin, and the result is subtracted from the experimental value and divided by the total uncertainties, statistic and systematic. These normalized residuals are squared and summed over all available data at each collision energy, and the resulting total  $\chi^2$  is minimized. Since the aim of the present work is to describe particle production in relativistic heavy-ion collision with a non-equilibrium statistical model, comparison with data is carried out only in the  $p_{\perp} \leq 4$  GeV region, outside which hard QCD interactions are expected to dominate over thermal effects. At high transverse momentum, a non-equilibrium statistical description such the one employed in this work cannot be expected to hold, and perturbative QCD approaches as in Refs. [76–78], have to be applied. The minimization process is carried out with the MATLAB routine `fminsearch.m`, based on the Nelder-Mead simplex algorithm [79]. Uncertainties of the parameter vector  $\theta$  are estimated with the square root of the covariance matrix diagonal, which is obtained by inverting the Hessian of  $\chi^2(\theta)$ . The latter is calculated numerically with the MATLAB suite `DERIVEST` [80].

The results of the parameter optimization for both LHC energies are shown in Table 4.1. While the transverse thermalization is almost instantaneous, the system remains very far from equilibration in the longitudinal direction, as indicate the relative small values of  $D_{\parallel}\Delta t$ , that can be compared to Fig. 4.3a for reference. In addition, the  $\chi^2$  optimization reaches the lower bound of  $\alpha = -1$  for both  $\sqrt{s_{\text{NN}}} = 2.76$  TeV and 5.02 TeV, corresponding to an almost null equilibration at  $y = 0$ . During the fitting process, as already argued in [63], it was verified that the parameters describing the transverse GFPS are highly correlated. In particular,

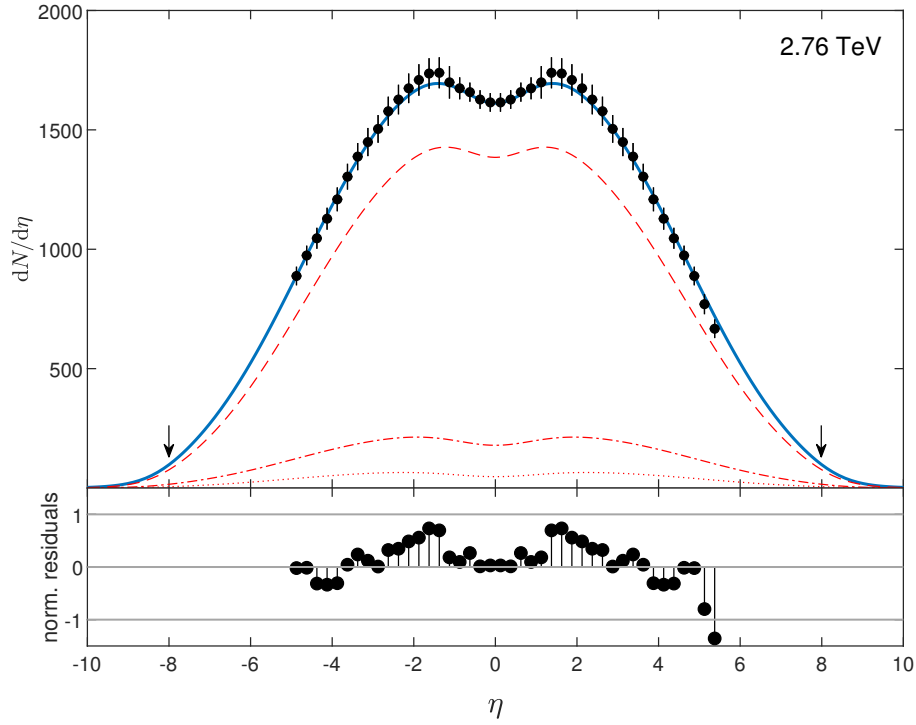


Figure 4.5: Comparison of the calculated marginal pseudorapidity charged-hadrons NDF  $dN/d\eta$  of central  $\sqrt{s_{\text{NN}}} = 2.76$  TeV Pb-Pb collisions to 0-5% ALICE data [25]. In the top panel, the solid blue curve indicates the total calculated particle yield, while the red dashed, dot-dashed, and dotted lines are the contributions of pions, kaons, and (anti)protons, respectively. The black dots are the experimental data points, with the vertical error bars including statistic and systematic error. The bins are smaller than the symbol size, and the black arrows mark the beam rapidity. The bottom panel shows the normalized residuals, as defined in the text, for every bin.

it was experienced that allowing for two exponents  $c$  and  $d$  was redundant, and that only the value of the product  $cd$  is relevant when stopping the fit at  $p_{\perp} = 4$  GeV. The degrees of freedom of the model were then reduced from seven to six by fixing the first exponent to the arbitrary value of  $c = 5$ . A questionable find of the optimization are the surprisingly high values of  $T$ , especially at the higher energy. A partial explanation for this fact is that  $T$  hardly influences the longitudinal direction, as was shown in Fig. 3.3, and only in a rapidity region not covered by the experimental data. In fact, the temperature determined in the previous iteration of the model [24], that assumed an almost identical equilibrium PDF in the longitudinal direction, was only 100 MeV. When considering the marginal transverse momentum PDF, the effect of varying  $T$  is clearly greater, as can be again verified from Fig. 3.3. It would be however a mistake to identify  $T$  as the physical temperature of the system, since the GFPS is not a (modified) thermal distribution.

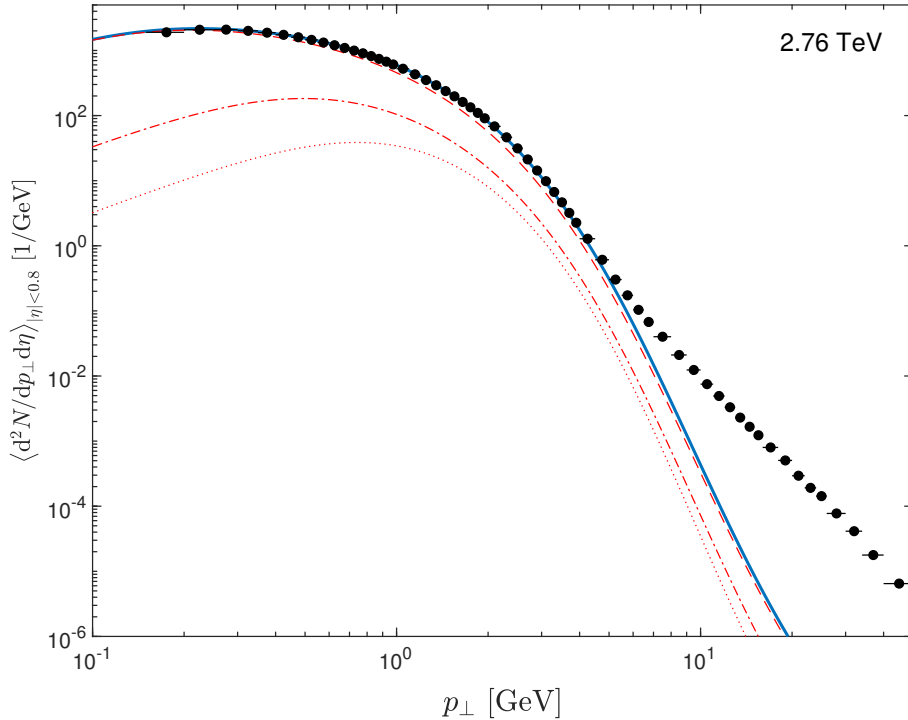


Figure 4.6: Comparison of the calculated joint produced charged-hadron spectrum  $d^2N/d\eta dp_\perp$  to 0-5% ALICE data [27] in  $\sqrt{s_{\text{NN}}} = 2.76$  TeV Pb-Pb central collisions, averaged over the  $|\eta| < 0.8$  slice and plotted against  $p_\perp$  on a log-log scale. The four curves represent the same quantities as in Fig. 4.5. Horizontal bars indicate the bin size, and experimental error bars are smaller than the symbols. See text for the deviation beyond  $p_\perp = 4$  GeV.

Albeit it has the physical dimension of a temperature,  $T$  should be seen as a phenomenological parameter of the transverse equilibrium distribution as  $b$ ,  $c$  and  $d$ . In fact,  $T$  is highly correlated with the parameter  $b$  via their ratio  $b/T$ , and the peculiar large values of  $T$  are paired with corresponding large values of  $b$ , and the associated uncertainties are quite large, especially at  $\sqrt{s_{\text{NN}}} = 5.02$  TeV. It would be desirable to conciliate the physical meaning that  $T$  assumes in the marginal longitudinal PDF with its role in the transverse GFPS, by incorporating the latter in a generalized thermal distribution of the form (3.17), but that is out of the scope of this work.

For  $\sqrt{s_{\text{NN}}} = 2.76$  TeV, the ALICE data set [25] contains measurements of the marginal pseudorapidity NDF in the  $-5 \leq \eta \leq 5.5$  window. The comparison of the model result with the data is presented in Fig. 4.5. In the top panel, the total particle yield is showed as a solid blue curve, along with the individual contributions of pions, kaons and protons as red dashed, dot-dashed, and dotted lines. As can be inferred by the normalized residuals shown in the bottom panel, the model describes the pseudorapidity spectrum very well, with only the rightmost data point

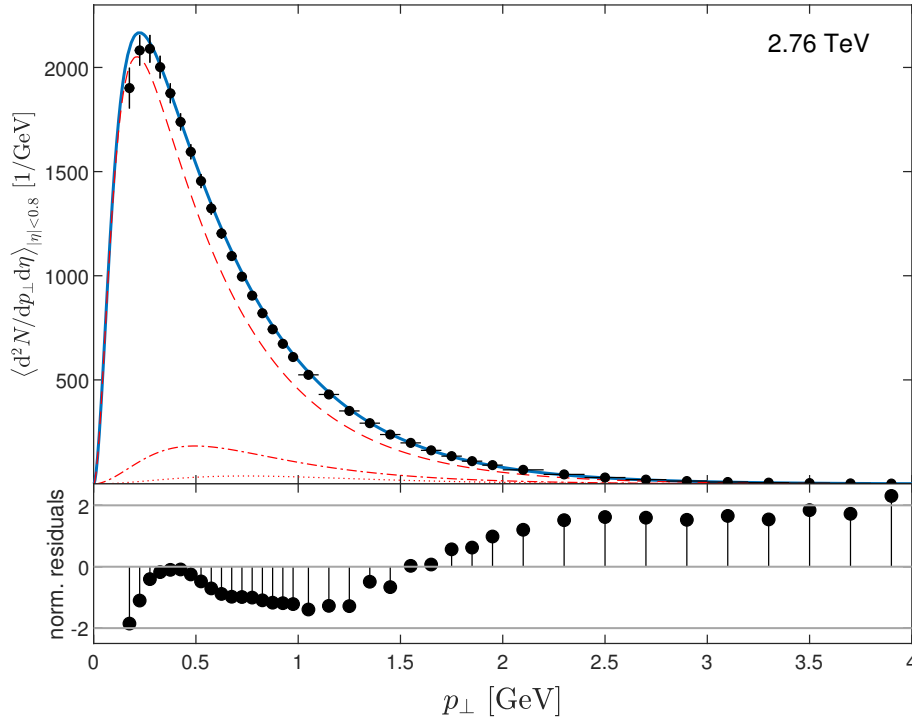


Figure 4.7: Same as Fig. 4.6, but restricted to the interval  $p_\perp < 4$  GeV and on a linear scale. Normalized residuals are shown in the bottom panel.

having an error exceeding one  $\sigma$ . In particular, allowing for rapidity-dependent  $D_Y$  produces a considerably better agreement with experiments in the midrapidity dip than the previous iteration of the model [24], where, due to the assumption of a constant diagonal diffusion, a too low particle yield was predicted at  $y = \eta = 0$ . In Figs. 4.6 and 4.7 the model predictions are compared with transverse momentum data from ALICE [27], obtained averaging over a  $|\eta| \leq 0.8$  pseudorapidity slice. Figure 4.6 shows the whole experimentally available transverse momentum range, up to  $p_\perp = 50$  GeV, in a log-log scale, with the total particle yield and the single species contributions represented as in Fig. 4.5. The model prediction clearly deviates from the experimental data beyond  $p_\perp = 4$  GeV, due to the fact that the subsequent transverse region was not included in the  $\chi^2$  minimization. A closer look at the fitted region is given in Fig. 4.7, where the comparison of the model to data is showed for  $p_\perp \leq 4$  GeV in a linear scale in the upper part. The corresponding normalized residuals in the bottom panel indicate a sensibly worse agreement to the experimental data than in the longitudinal direction. The last data set for 2.76 TeV Pb-Pb collisions was produced by the ATLAS experiment [28], and contains two-dimensional measurements of charged-hadron production in the window given by  $0 \leq \eta \leq 2$  and  $0.5 \leq p_\perp \leq 150$  GeV. In Fig. 4.8 the model calculated NDF  $d^2N/d\eta dp_\perp$  is showed as a two-dimensional contour plot with the logarithmic color scale on the right, and the normalized residuals are represented as superimposed

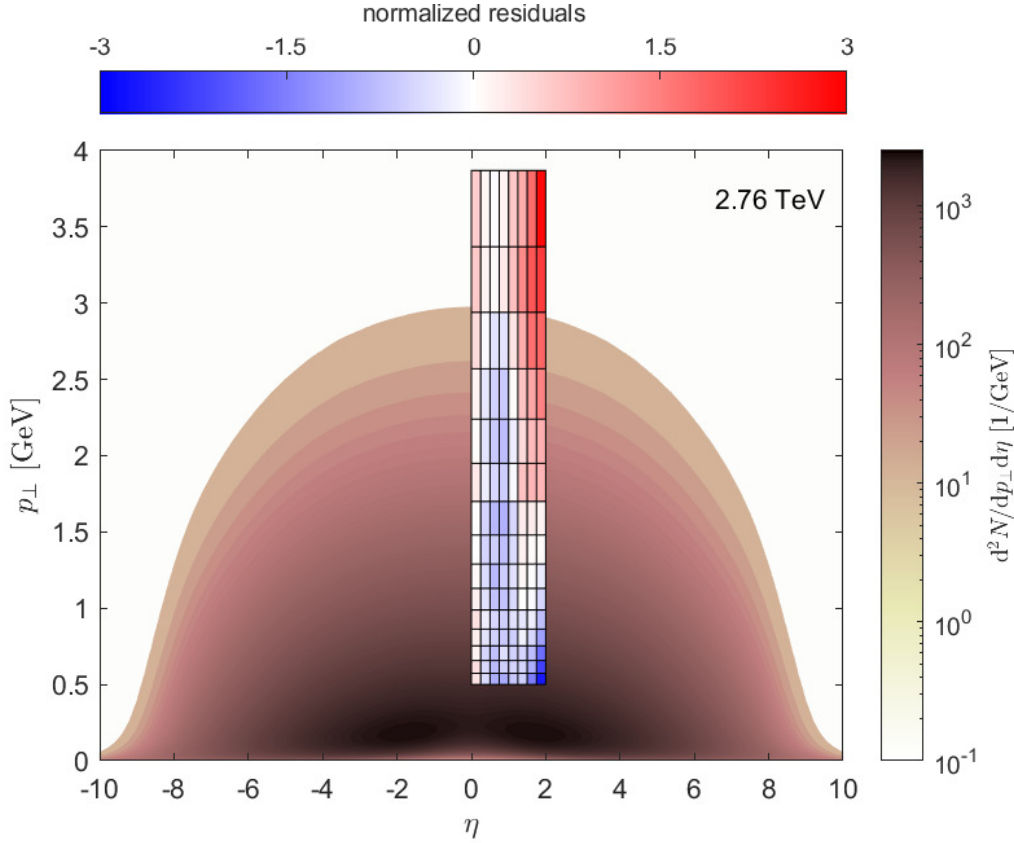


Figure 4.8: Joint two-dimensional spectrum of produced charged hadrons in  $\sqrt{s_{\text{NN}}} = 2.76$  TeV Pb-Pb central collisions, compared to 0-5% ATLAS data [28]. The logarithmic color scale on the right refers to the calculated value of  $d^2N/dp_{\perp}d\eta$ , and the linear color scale at the top refers to the normalized residuals - data minus model prediction divided by total uncertainty - represented as rectangles the size of the corresponding experimental bin.

rectangular bins with the linear color scale on top. Figure 4.9 present the same results, but plotted  $p_{\perp}$ -binwise against pseudorapidity, with each curve in  $\eta$  obtained averaging the model calculated differential yield over a  $p_{\perp}$  bin. The model gives an overall good description of the data, with the exception of the outer pseudorapidity region  $1.5 \leq \eta \leq 2$ , where the experimental measurements strongly deviates from the prediction, with a discrepancy of more than  $2.5\sigma$  for the two worst described bins. The non monotonic behavior of the data in that pseudorapidity range in the low- $p_{\perp}$  bins cannot be accurately described with the assumption of a diagonal diffusivity, nor is an effect of the Jacobian transformation from the  $(h, y)$  coordinate space, and a more complex model would probably be needed to address this feature. It is however reasonable to ask whether this is a real physical characteristic of hadron production or an underestimation of the systematic error of the experiment, especially when comparing it to the ALICE marginal pseudorapidity data [25, 26],

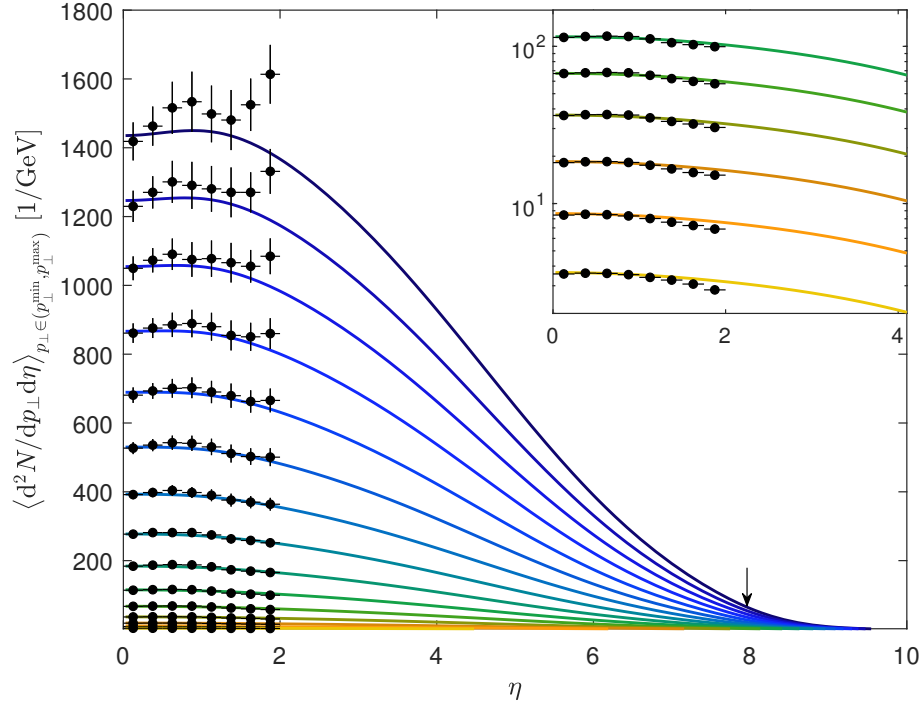


Figure 4.9: Joint two-dimensional spectrum of produced charged hadrons in  $\sqrt{s_{\text{NN}}} = 2.76$  TeV Pb-Pb central collisions, compared to 0-5% ATLAS data [28], averaged over experimental  $p_\perp$  bins from  $p_\perp = 0.5$  GeV (top curve) to  $p_\perp = 3.87$  GeV (bottom curve) and plotted against positive  $\eta$ . The insert shows in detail the six lowest curves, from  $p_\perp = 1.7$  GeV to  $p_\perp = 3.87$  GeV, on a vertical logarithmic scale. Vertical and horizontal bars indicates the total uncertainties and the bin sizes in the  $\eta$  direction. The black arrow marks the beam rapidity.

that show a strikingly smoother trend at both 2.76 and 5.02 TeV.

The calculated marginal pseudorapidity distribution for Pb-Pb collision at  $\sqrt{s_{\text{NN}}} = 5.02$  TeV is compared to ALICE data [26] covering the midrapidity window  $-3.5 \leq \eta \leq 5$  in Fig. 4.10. As for the lower energy, the total hadron production  $dN/d\eta$  is showed as a solid blue line, while the partial contributions of pions, kaons and protons as red dashed, dot-dashed, and dotted lines. Figures 4.11 and 4.12 present the model prediction in the transverse direction, obtained averaging  $d^2N/d\eta dp_\perp$  over the  $|\eta| \leq 0.8$  pseudorapidity slice, in comparison with ALICE data [27]. The first image comprehends the whole measured  $p_\perp$  range plotted on a log-log scale, while the second analyzes only the  $p_\perp \leq 4$  GeV fitted region on a linear scale, and shows the associate normalized residuals. The spectrum is qualitatively similar to that of the 2.76 TeV collision energy, apart from the expected higher total number of produced particles. Due to the unusual course of the 5.02 TeV  $dN/d\eta$  ALICE measurements around  $|\eta| \approx 4$  and the lack of a measured joint spectrum outside the midrapidity region, it proved difficult to obtain a reasonable fit result for the longitudinal diffusivity. The  $\chi^2$  minimization tried to compensate for the these

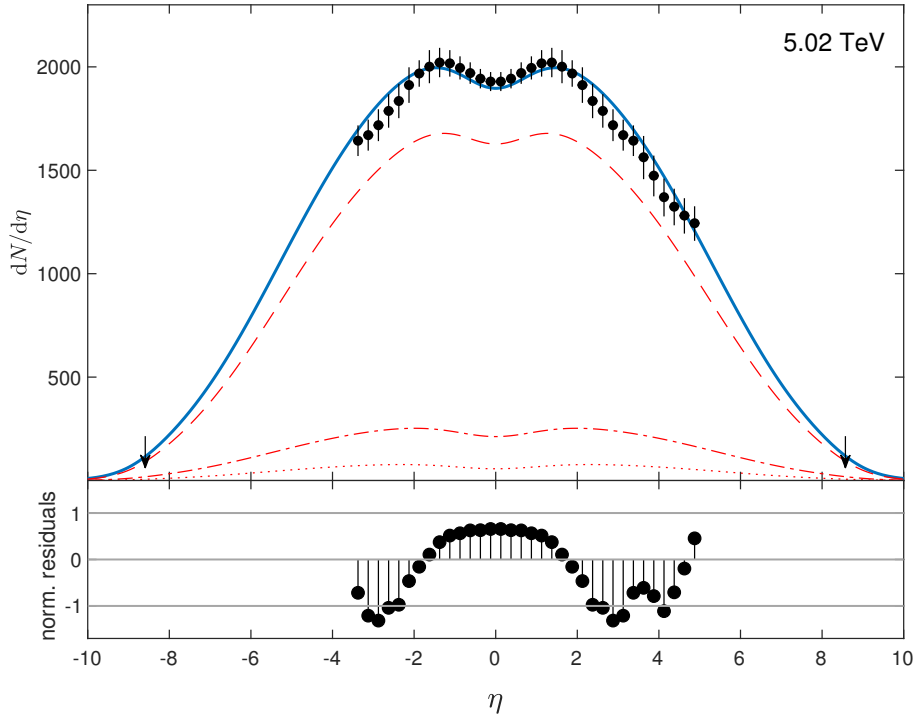


Figure 4.10: Comparison of the calculated marginal pseudorapidity charged-hadron NDF  $dN/d\eta$  of central  $\sqrt{s_{\text{NN}}} = 5.02$  TeV Pb-Pb collisions to 0-5% ALICE data [26] (black points). The top panel shows the total produced hadrons (solid curve) and the contribution of pions (dashed), kaons (dot-dashed), and (anti)protons (dotted). Horizontal bars represent the total experimental errors, the bins are smaller than the symbol size, and the black arrows mark the beam rapidity. The bottom panel shows the normalized residuals for every bin.

dubious features in the data, resulting in an overfitted set of parameters predicting a hardly physically justifiable high particle production at intermediate-to-high rapidity. To address this problem, already encountered by Hoelck & Wolschin [24], the much clearer 2.76 TeV result for  $D_{\parallel}\Delta t$  is extrapolated to the higher energy by scaling it with the beam rapidity, based on the earlier finding by Röhrscheid & Wolschin [81] that the width of the marginal pseudorapidity distribution is in good approximation proportional to the logarithm of the respective center-of-mass energy. Despite having reduced the free parameters by fixing  $D_{\parallel}\Delta t$ , the fitted model provides a satisfactory description of the experimentally measured spectrum in both the longitudinal and transverse directions.

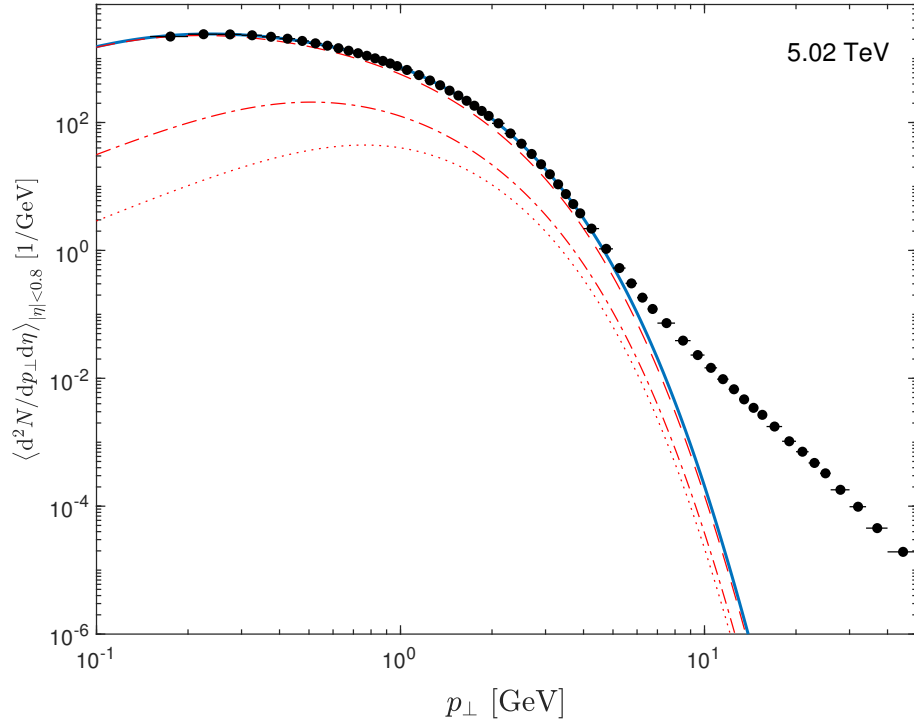


Figure 4.11: Comparison of the calculated joint produced charged-hadron spectrum  $d^2N/d\eta dp_{\perp}$  to 0-5% ALICE data [27] in  $\sqrt{s_{\text{NN}}} = 5.02$  TeV Pb-Pb central collisions, averaged over the  $|\eta| < 0.8$  slice and plotted against  $p_{\perp}$  on a log-log scale. See text for deviation above 4 GeV.

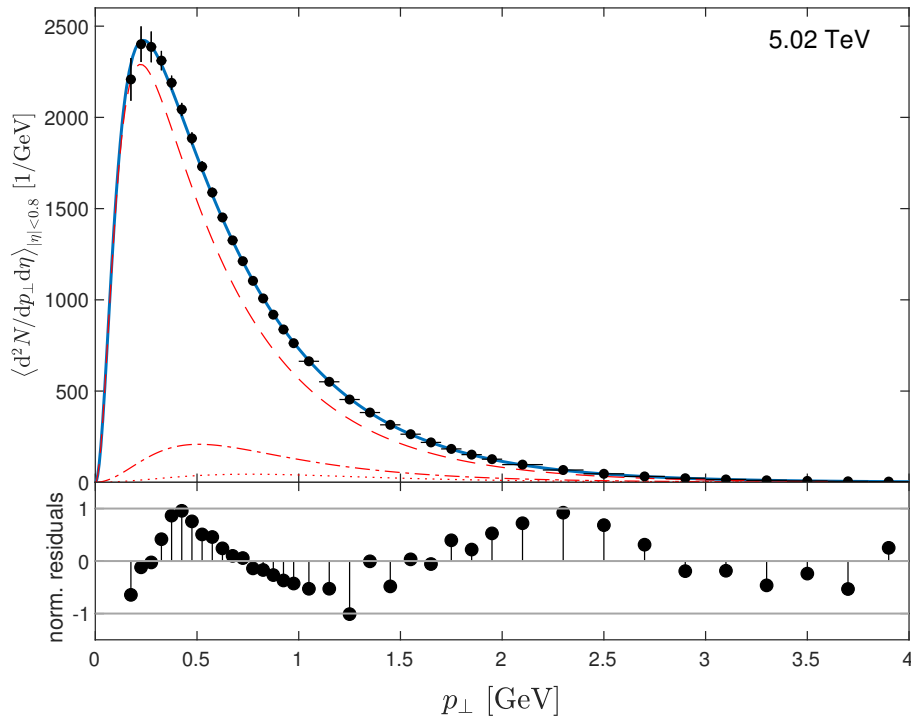


Figure 4.12: Same as Fig. 4.11, but restricted to the interval  $p_{\perp} < 4$  GeV and on a linear scale. Normalized residuals are shown in the bottom panel.



## 4.4 Prediction of the current LHC run

While this document is being drafted, the third run of LHC is undergoing, and the ALICE experiment is collecting data of Pb-Pb collisions at  $\sqrt{s_{\text{NN}}} = 5.36$  TeV. It is then interesting to use the discussed drift-diffusion model to make a prediction of the charged-hadron spectra at this energy. To do so, since no data are yet available, the free parameters of the model at  $\sqrt{s_{\text{NN}}} = 5.36$  TeV have to be meaningfully extrapolated from the two fitted lower energies. Regarding the approach to thermalization in the longitudinal direction, the value of  $D_Y \Delta t$  can be obtained by scaling it with the beam rapidity, as already done for  $\sqrt{s_{\text{NN}}} = 5.02$ . Since  $\alpha$  reaches the lower boundary of  $-1$  for both the lower energies, this is assumed to be the case at 5.36 TeV as well. Regarding the GFPS parameters describing the transverse spectrum, it is more difficult to infer a scaling with the energy. Apart from the condition  $c = 5$  that is maintained,  $T, b$  and  $d$  are also assumed proportional to  $y_b$ . While, apart for the increasing trend at the two lower energies, no physical justification for such a scaling is formulated here, it is a reasonable assumption that being  $\sqrt{s_{\text{NN}}} = 5.36$  a relatively limited increase in energy from 5.02 TeV, a linear extrapolation should roughly provide an adapt parameter set. The last step before making a prediction is to fix the total number of charged hadrons  $N$ . In an investigation of the central and fragmentation sources yield in heavy-ion collisions at RHIC and LHC energies, Wolschin [20] formulated a phenomenological scaling of the gluon-gluon total charged-hadron yield with the cube of the beam rapidity, that is here used to predict  $N$  at 5.36 TeV. The extrapolated parameter set is reported in Tab. 4.1, and the resulting spectra in the longitudinal and transverse direction is shown in Figs. 4.13 and. 4.14. In the same investigation, it was found that in good approximation the particle yield at mid-rapidity for different total energies should be given by

$$\left. \frac{dN}{d\eta} \right|_{\eta=0} \approx 1150 \left( \frac{s_{\text{NN}}}{s_0} \right)^{0.165}, \quad (4.6)$$

with  $s_0 = 1$  TeV<sup>2</sup>. The predictions of this phenomenological law agree with experimental data at both LHC energies, but deviate from the model prediction of the 5.36 TeV longitudinal spectrum. In Fig. 4.15, the marginal pseudorapidity hadron yield of the drift-diffusion model is reported for all three energies.

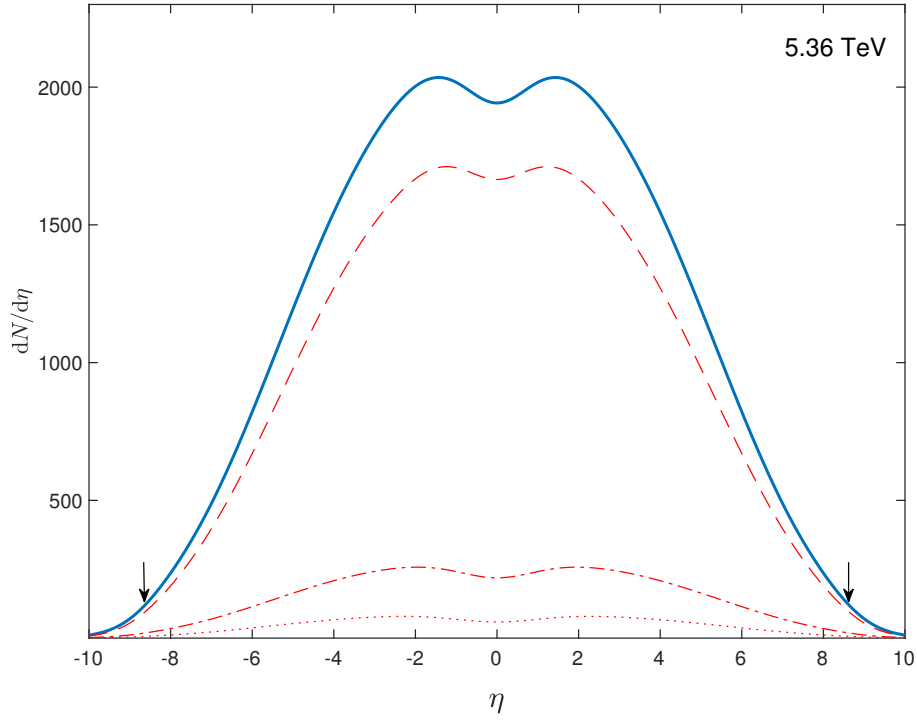


Figure 4.13: Predicted marginal pseudorapidity  $dN/d\eta$  of produced charged hadrons in central  $\sqrt{s_{NN}} = 5.36$  TeV Pb-Pb collisions. The curves are the total produced hadrons (solid) and the contribution of pions (dashed), kaons (dot-dashed), and (anti)protons (dotted).

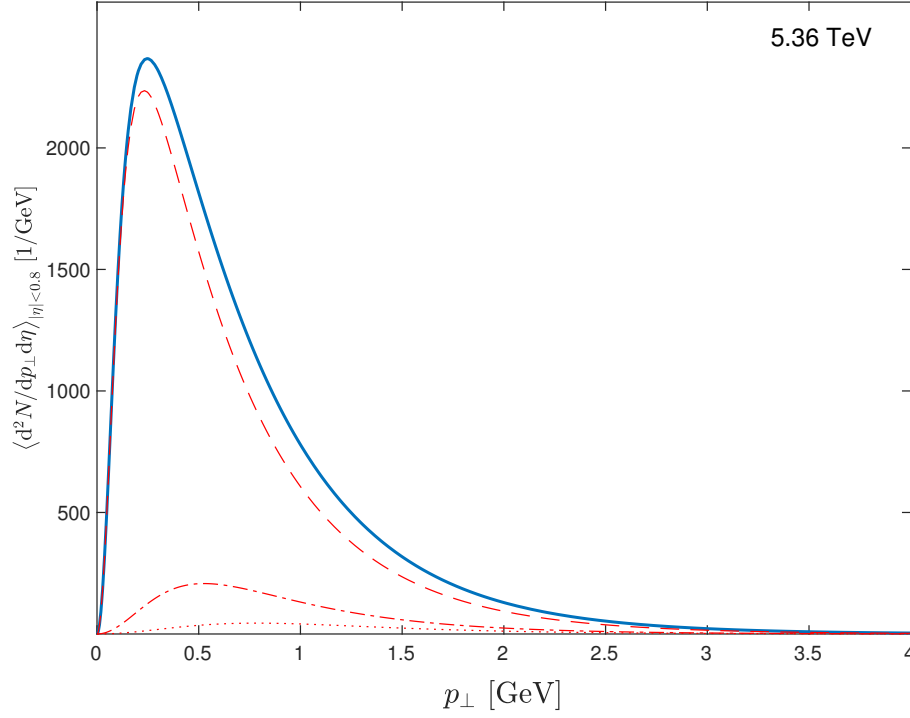


Figure 4.14: Predicted joint spectrum  $d^2N/d\eta dp_\perp$  of produced charged hadrons in  $\sqrt{s_{NN}} = 5.36$  TeV Pb-Pb central collisions, averaged over the  $|\eta| < 0.8$  slice and plotted against  $p_\perp$ .

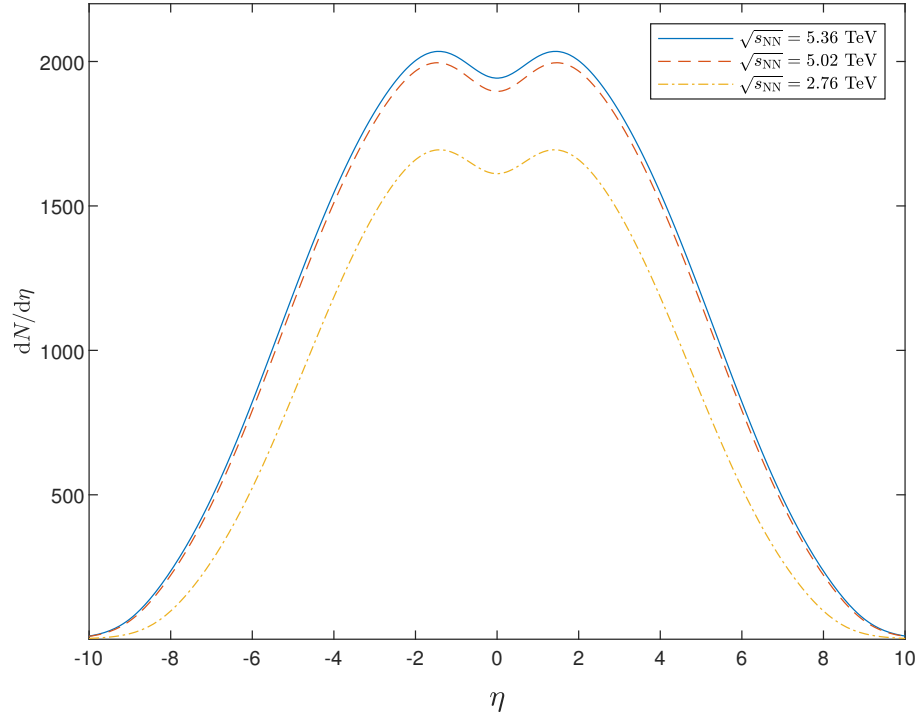


Figure 4.15: Predicted marginal pseudorapidity  $dN/d\eta$  of produced charged hadrons in central  $\sqrt{s_{NN}} = 5.36$  TeV Pb-Pb collisions (solid curve) compared to the result at  $\sqrt{s_{NN}} = 5.02$  TeV (dashed) and  $\sqrt{s_{NN}} = 2.76$  TeV (dot-dashed).



# Chapter 5

## Discussion

A spectral eigenfunction decomposition of the Fokker-Planck operator derived from a drift-diffusion model of produced charged-hadron thermalization in relativistic heavy-ion collisions was implemented. The representation of the FPO is based on a polynomial basis constructed with an orthonormality relation with respect to the stationary solution of the FPE, which is the first eigenfunction of the associated differential operator. When considering the central fireball, which is the main source of particle production through gluon-gluon interactions at LHC energies, such a spectral method is successfully applied, and the convergence of the solution is fast in the basis dimension. On the contrary, it proved difficult to employ the same spectral representation to solve the FPE of the forward and backward fragmentation sources, due to the inadequacy of the orthogonal basis to describe their initial condition.

The accuracy of the spectral solution scheme allows to compare the calculated spectrum in a large transverse momentum region. The fit to experimental data from the ALICE and ATLAS collaborations is however limited to  $p_{\perp} < 4$  GeV, since at larger transverse momentum a perturbative QCD description is expected to take over the produced charged-hadron distribution from the non-equilibrium statistical approach used in this work. Furthermore, the previous iteration of the relativistic drift-diffusion model is enriched with a rapidity-dependent diffusion, which produces a better description of the longitudinal spectrum in the mid-rapidity region. The total reduced  $\chi^2$  indicates a significant prediction at both  $\sqrt{s_{NN}} = 2.76$  and 5.02 TeV, although some features of the joint spectra at the lower energy are not properly accounted for by the assumptions of the model.

Finally, the model's free parameters have been extrapolated from the two fitted energies to  $\sqrt{s_{NN}} = 5.36$  TeV, and a prediction of the charged-hadron spectrum for the current LHC run in the longitudinal and transverse directions has been presented.

Future developments of the model should include a microscopical derivation of the diffusivity rapidity dependence, and possibly consider a transverse dependence

as well. Including off-diagonal components in the diffusion matrix could also provide a better physical representation of charged-hadron production, but is certainly more challenging to implement in the present solution scheme. An extension to non-central collisions would require to also consider the third spatial dimension, which would be problematic to tackle with spectral methods. The inclusion of the fragmentation sources is essential to describe baryon stopping, and should be addressed by employing a different representation of the FPO.

Lastly, it would be beneficial to integrate the longitudinal and transverse marginal asymptotic states into a coherent modified thermal distribution, to gain a better physical insight of their free parameters.

# Glossary

<b>FPE</b> Fokker-Planck Equation . . . . .	ii, 1–3, 14–17, 19, 21, 26, 34, 35, 37, 38, 42, 53, 55
<b>CGC</b> Color-Glass Condensate . . . . .	29, 38
<b>COM</b> Center-of-Momentum Frame . . . . .	23, 24, 29
<b>DIS</b> Deep Inelastic Scattering . . . . .	29, 30, 38
<b>FDR</b> Fluctuation-Dissipation Relation . . . . .	2, 17, 26, 28, 33, 35, 41, 42
<b>FPO</b> Fokker-Planck Operator . . . . .	15, 17– 19, 26, 27, 33–38, 41, 53–55
<b>FWHM</b> Full Width at Half Maximum . . . . .	32
<b>GFPS</b> Generalized Fokker-Planck Solution . . . . .	32, 43, 44, 49
<b>LHC</b> Large Hadron Collider . . . . .	1, 3, 21, 27, 30, 32, 37, 39, 42, 43, 49, 52, 53
<b>NDF</b> Number Density Function . . . . .	2, 25, 40, 44–46, 49, 55
<b>ODE</b> Ordinary Differential Equation . . . . .	11
<b>PDF</b> Probability Density Function . . . . .	1, 3, 8– 10, 12–15, 22, 25, 28–32, 37–44, 55
<b>PMF</b> Probability Mass Function . . . . .	8, 10, 12
<b>QCD</b> Quantum Chromodynamics . . . . .	1, 2, 29, 43

*Glossary*

<b>QGP</b> Quark-Gluon Plasma . . . . .	1, 22
<b>RHIC</b> Relativistic Heavy Ion Collider . . . . .	1, 2, 52
<b>SDE</b> Stochastic Differential Equation . . . . .	12, 13, 22
<b>SPS</b> Super Proton Synchrotron . . . . .	2
<b>RDM</b> Relativistic Diffusion Model . . . . .	2



# List of Figures

1.1	Detected particle shower of a single Pb-Pb collision. . . . .	2
3.1	Space-time diagram of a heavy-ion collision. . . . .	23
3.2	Initial PDF of the central gluon-gluon source. . . . .	28
3.3	Asymptotic marginal PDFs for pions production. . . . .	30
4.1	Spectral convergence of the FPE. . . . .	38
4.2	Fragmentation initial and asymptotic PDF. . . . .	39
4.3	Time evolution of the marginal rapidity NDF. . . . .	40
4.4	Drift coefficient $\mu_Y$ of the marginal rapidity adimensional FPO. . . .	41
4.5	Comparison of the calculated pseudorapidity spectrum to ALICE data for $\sqrt{s_{NN}} = 2.76$ TeV. . . . .	44
4.6	Joint spectrum averaged over an $\eta$ slice compared to ALICE data for $\sqrt{s_{NN}} = 2.76$ TeV. . . . .	45
4.7	Detail of the joint spectrum averaged over an $\eta$ slice compared to ALICE data for $\sqrt{s_{NN}} = 2.76$ TeV. . . . .	46
4.8	Joint two-dimensional spectrum compared to ATLAS data for $\sqrt{s_{NN}} = 2.76$ TeV. . . . .	47
4.9	Joint two-dimensional spectrum, plotted $p_{\perp}$ -binwise, compared to ATLAS data for $\sqrt{s_{NN}} = 2.76$ TeV. . . . .	48
4.10	Comparison of the calculated pseudorapidity spectrum to ALICE data for $\sqrt{s_{NN}} = 5.02$ TeV. . . . .	49
4.11	Joint spectrum averaged over an $\eta$ slice compared to ALICE data for $\sqrt{s_{NN}} = 5.02$ TeV. . . . .	50
4.12	Detail of the joint spectrum averaged over an $\eta$ slice compared to ALICE data for $\sqrt{s_{NN}} = 5.02$ TeV. . . . .	50
4.13	Predicted marginal pseudorapidity spectrum for $\sqrt{s_{NN}} = 5.36$ TeV. . .	52
4.14	Predicted $\eta$ -averaged joint spectrum for $\sqrt{s_{NN}} = 5.36$ TeV. . . . .	53
4.15	Comparison of marginal pseudorapidity spectra for all energies. . . .	53

## *List of Figures*

# References

1. Einstein, A. *Über die von der molekularkinetischen Theorie der Wärme geforderte Bewegung von in ruhenden Flüssigkeiten suspendierten Teilchen*. Annalen Phys. **322**, 549–560 (1905).
2. Einstein, A. *Zur Theorie der Brownschen Bewegung*. Annalen Phys. **324**, 371–381 (1906).
3. Smoluchowski, M. *Zur kinetischen Theorie der Brownschen Molekularbewegung und der Suspensionen*. Annalen Phys. **326**, 756–780 (1906).
4. Smoluchowski, M. *Über Brownsche Molekularbewegung unter Einwirkung äußerer Kräfte und deren Zusammenhang mit der verallgemeinerten Diffusionsgleichung*. Annalen Phys. **353**, 1103–1112 (1916).
5. Langevin, P. *Sur la théorie du mouvement brownien*. Com. R. Heb. S. Acad. Sci. **146**, 530–533 (1908).
6. Uhlenbeck, G. E. & Ornstein, L. S. *On the Theory of the Brownian Motion*. Phys. Rev. **36**, 823–841 (1930).
7. Markov, A. A. *Rasprostranenie zakona bolshikh chisel na velichiny zavisyashchie drug ot druga*. Izv. Fiz.-Mat. Obs. Kazan. Univ. **15**, 135–156 (1906).
8. Wiener, N. *Differential-Space*. J. Math. Phys. **2**, 131–174 (1923).
9. Chapman, S. *On the Brownian displacements and thermal diffusion of grains suspended in a non-uniform fluid*. Proc. Royal Soc. London. A **119**, 34–54 (1928).
10. Kolmogorov, A. *Über die analytischen Methoden in der Wahrscheinlichkeitsrechnung*. Math. Annalen **104**, 415–458 (1931).
11. Kolmogorov, A. *Grundbegriffe der Wahrscheinlichkeitsrechnung* (Springer, 1933).
12. Itô, K. *Stochastic integral*. Proc. Imp. Acad. **20**, 519–524 (1944).
13. Debbasch, F., Mallick, K. & Rivet, J. P. *Relativistic Ornstein–Uhlenbeck Process*. J. Stat. Phys. **88**, 945–966 (1997).

## References

14. Dunkel, J. & Hänggi, P. *Theory of relativistic Brownian motion: The  $(1 + 1)$ -dimensional case*. Phys. Rev. E **71**, 016124 (2005).
15. Dunkel, J. & Hänggi, P. *Theory of relativistic Brownian motion: The  $(1 + 3)$ -dimensional case*. Phys. Rev. E **72**, 036106 (2005).
16. Fokker, A. D. *Die mittlere Energie rotierender elektrischer Dipole im Strahlungsfeld*. Annalen Phys. **348**, 810–820 (1914).
17. Planck, M. *Über einen Satz der statistischen Dynamik und seine Erweiterung in der Quantentheorie*. **24**, 324–341 (1917).
18. Wolschin, G. *Relativistic diffusion model*. Eur. Phys. J. A - Hadron. Nucl. **5**, 85–90 (1999).
19. Biyajima, M., Ide, M., Mizoguchi, T. & Suzuki, N. *Scaling Behavior of  $(N_{ch})^{-1} dN_{ch}/d\eta$  at by the PHOBOS Collaboration and Its Implication: A Possible Explanation Employing the Ornstein-Uhlenbeck Process*. Prog. Theor. Phys. **108**, 559–569 (2002).
20. Wolschin, G. *Ultraviolet energy dependence of particle production sources in relativistic heavy-ion collisions*. Phys. Rev. C **91**, 014905 (2015).
21. Mehtar-Tani, Y. & Wolschin, G. *Baryon Stopping as a New Probe of Geometric Scaling*. Phys. Rev. Lett. **102**, 182301 (2009).
22. Mehtar-Tani, Y. & Wolschin, G. *Baryon stopping and saturation physics in relativistic collisions*. Phys. Rev. C **80**, 054905 (2009).
23. Hoelck, J. & Wolschin, G. *Baryon stopping as a relativistic Markov process in phase space*. Phys. Rev. Res. **2**, 033409 (2020).
24. Hoelck, J. & Wolschin, G. *Cylindrically symmetric diffusion model for relativistic heavy-ion collisions*. Submitt. to Annalen Phys. (2023).
25. Abbas, E. *et al.* *Centrality dependence of the pseudorapidity density distribution for charged particles in Pb–Pb collisions at  $\sqrt{s_{NN}} = 2.76$  TeV*. Phys. Lett. B **726**, 610–622 (2013).
26. Adam, J. *et al.* *Centrality dependence of the pseudorapidity density distribution for charged particles in Pb–Pb collisions at  $\sqrt{s_{NN}} = 5.02$  TeV*. Phys. Lett. B **772**, 567–577 (2017).
27. Acharya, S. *et al.* *Transverse momentum spectra and nuclear modification factors of charged particles in pp, p-Pb and Pb-Pb collisions at the LHC*. J. High Energy Phys. **2018**, 1–33 (2018).
28. Aad, G. *et al.* *Measurement of charged-particle spectra in Pb+Pb collisions at  $\sqrt{s_{NN}} = 2.76$  TeV with the ATLAS detector at the LHC*. J. High Energy Phys. **2015**, 50 (2015).

29. Gardiner, C. *Stochastic Methods: A Handbook for the Natural and Social Sciences* (Springer Berlin, Heidelberg, 2009).
30. Pavliotis, G. *Stochastic Processes and Applications: Diffusion Processes, the Fokker-Planck and Langevin Equations* (Springer New York, 2014).
31. Hänggi, P. & Thomas, H. *Stochastic processes: Time evolution, symmetries and linear response*. Phys. Reports **88**, 207–319 (1982).
32. Schwarz, U. *Stochastic dynamics*. 2019.
33. Risken, H. *The Fokker-Planck Equation: Methods of Solution and Applications* (Springer Berlin, Heidelberg, 1996).
34. Donsker, M. D. *Justification and Extension of Doob's Heuristic Approach to the Kolmogorov-Smirnov Theorems*. The Ann. Math. Stat. **23**, 277–281 (1952).
35. Stratonovich, R. L. *A New Representation for Stochastic Integrals and Equations*. SIAM J. on Control **4**, 362–371 (1966).
36. Fisk, D. L. *Quasi-martingales*. Trans. Am. Math. Soc. **120**, 369–389 (1965).
37. Kramers, H. *Brownian motion in a field of force and the diffusion model of chemical reactions*. Physica **7**, 284–304 (1940).
38. Moyal, J. E. *Stochastic Processes and Statistical Physics*. J. Royal Stat. Soc. Ser. B (Methodological) **11**, 150–210 (1949).
39. Ji, M., Shen, Z. & Yi, Y. *Convergence to Equilibrium in Fokker-Planck Equations*. J. Dyn. Differ. Equations **31**, 1591–1615 (1, 2019).
40. Łopuszański, J. *Relativisierung der Theorie der Stochastischen Prozesse*. Acta Physica Polonica **12**, 87–99 (1953).
41. Dudley, R. M. *Lorentz-invariant Markov processes in relativistic phase space*. Ark. Mat. **6**, 241–268 (1966).
42. Hakim, R. *Relativistic Stochastic Processes*. J. Math. Phys. **9**, 1805–1818 (1968).
43. Dunkel, J., Hänggi, P. & Hilbert, S. *Non-local observables and lightcone-averaging in relativistic thermodynamics*. Nat. Phys. **5**, 741–747 (2009).
44. Braun-Munzinger, P. & Dönigus, B. *Loosely-bound objects produced in nuclear collisions at the LHC*. Nuc. Phys. A **987**, 144–201 (2019).
45. Bjorken, J. D. *Highly relativistic nucleus-nucleus collisions: The central rapidity region*. Phys. Rev. D **27**, 140–151 (1983).
46. Hagedorn, R. *Statistical thermodynamics of strong interactions at high energies*. Nuovo Cimento, Suppl. **3**, 147–186 (1965).

## References

47. Wolschin, G., Biyajima, M., Mizoguchi, T. & Suzuki, N. *Time evolution of relativistic  $d + Au$  and  $Au + Au$  collisions*. Annalen Phys. **518**, 369–378 (2006).
48. Wolschin, G. *Diffusion in relativistic systems*. Prog. Particle Nuc. Phys. **59**, 374–382 (2007).
49. Kellers, B. & Wolschin, G. *Limiting fragmentation at LHC energies*. Prog. Theor. Exp. Phys. **2019**, 053D03 (2019).
50. Gribov, L., Levin, E. & Ryskin, M. *Semihard processes in QCD*. Phys. Reports **100**, 1–150 (1983).
51. Mueller, A. & Qiu, J. *Gluon recombination and shadowing at small values of  $x$* . Nuc. Phys. B **268**, 427–452 (1986).
52. Blaizot, J. & Mueller, A. *The early stage of ultra-relativistic heavy ion collisions*. Nuc. Phys. B **289**, 847–860 (1987).
53. McLerran, L. & Venugopalan, R. *Computing quark and gluon distribution functions for very large nuclei*. Phys. Rev. D **49**, 2233–2241 (1994).
54. Acharya, S., Adamová, D., Adler, A. & Adolfsson, J. *Characterizing the initial conditions of heavy-ion collisions at the LHC with mean transverse momentum and anisotropic flow correlations*. Phys. Lett. B **834**, 137393 (2022).
55. Golec-Biernat, K. & Wüsthoff, M. *Saturation effects in deep inelastic scattering at low  $Q^2$  and its implications on diffraction*. Phys. Rev. D **59**, 014017 (1998).
56. Kharzeev, D., Levin, E. & Nardi, M. *Color glass condensate at the LHC: hadron multiplicities in  $pp$ ,  $pA$  and  $AA$  collisions*. Nuc. Phys. A **747**, 609–629 (2005).
57. Cubero, D., Casado-Pascual J. and Dunkel, J., Talkner, P. & Hänggi, P. *Thermal Equilibrium and Statistical Thermometers in Special Relativity*. Phys. Rev. Lett. **99**, 170601 (2007).
58. Jüttner, F. *Das Maxwellsche Gesetz der Geschwindigkeitsverteilung in der Relativtheorie*. Annalen Phys. **339**, 856–882 (1911).
59. Schnedermann, E., Sollfrank, J. & Heinz, U. *Thermal phenomenology of hadrons from 200A GeV S+S collisions*. Phys. Rev. C **48**, 2462–2475 (1993).
60. Michael, C. & Vanryckeghem, L. *Consequences of momentum conservation for particle production at large transverse momentum*. J. Phys. G: Nuclear Phys. **3**, L151 (1977).
61. Hagedorn, R. *Multiplicities,  $p_T$  Distributions and the Expected Hadron  $\rightarrow$  Quark - Gluon Phase Transition*. Riv. Nuovo Cim. **6N10**, 1–50 (1983).
62. Aamodt, K. & et al. *Production of pions, kaons and protons in  $pp$  collisions at  $\sqrt{s} = 900$  GeV with ALICE at the LHC*. Eur. Phys. J. C **71**, 1655 (2011).

63. Zheng, H., Zhu, X., Zhu, L. & Bonasera, A. *Systematic investigation of the particle spectra in heavy-ion collisions at the Large Hadron Collider*. Mod. Phys. Lett. A **35**, 2050177 (2020).
64. Shizgal, B. D. *Spectral Methods in Chemistry and Physics: Spectral and Pseudospectral Methods of Solution of the Fokker-Planck and Schrödinger Equations*, 331–410 (Springer Dordrecht, 2015).
65. Trefethen, L. N. *Spectral Methods in MATLAB* (Society for Industrial and Applied Mathematics, 2000).
66. Davis, P. J. & Rabinowitz, P. *Methods of Numerical Integration*. 628 pp. (Academic Press, 10, 2014).
67. Gautschi, W. *Orthogonal polynomials: Constructive theory and applications*. J. Comput. Appl. Math. **12-13**, 61–76 (1985).
68. Gautschi, W. *Algorithm 726: ORTHPOL - a Package of Routines for Generating Orthogonal Polynomials and Gauss-Type Quadrature Rules*. ACM Trans. Math. Softw. **20**, 21–62 (1994).
69. Blackmore, R. & Shizgal, B. *Discrete-ordinate method of solution of Fokker-Planck equations with nonlinear coefficients*. Phys. Rev. A **31**, 1855–1868 (1985).
70. Shizgal, B. D. & Chen, H. *The quadrature discretization method (QDM) in the solution of the Schrödinger equation with nonclassical basis functions*. The J. Chem. Phys. **104**, 4137–4150 (1996).
71. Leung, K., Shizgal, B. D. & Chen, H. *The Quadrature Discretization Method (QDM) in comparison with other numerical methods of solution of the Fokker-Planck equation for electron thermalization*. J. Math. Chem. **24**, 291–319 (1998).
72. Shizgal, B. D. *Pseudospectral Solution of the Fokker-Planck Equation with Equilibrium Bistable States: the Eigenvalue Spectrum and the Approach to Equilibrium*. J. Stat. Phys. **164** (2016).
73. Schulze-Halberg, A. *Darboux transformations for (1+2)-dimensional Fokker-Planck equations with constant diffusion matrix*. J. Math. Phys. **53**, 103519 (2012).
74. Abelev, B. et al. *Centrality dependence of  $\pi$ ,  $K$ , and  $p$  production in Pb-Pb collisions at  $\sqrt{s_{NN}} = 2.76$  TeV*. Phys. Rev. C **88**, 044910 (2013).
75. Acharya, S. et al. *Production of charged pions, kaons, and (anti-)protons in Pb-Pb and inelastic pp collisions at  $\sqrt{s_{NN}} = 5.02$  TeV*. Phys. Rev. C **101**, 044907 (2020).

## References

- 76. Baier, R., Dokshitzer, Y., Mueller, A., Peigné, S. & Schiff, D. *Radiative energy loss and  $p_{\perp}$ -broadening of high energy partons in nuclei*. Nuclear Phys. B **484**, 265–282 (1997).
- 77. Guo, X. & Wang, X.-N. *Multiple Scattering, Parton Energy Loss, and Modified Fragmentation Functions in Deeply Inelastic  $eA$  Scattering*. Phys. Rev. Lett. **85**, 3591–3594 (2000).
- 78. Burke, K. M. *et al.* *Extracting the jet transport coefficient from jet quenching in high-energy heavy-ion collisions*. Phys. Rev. C **90**, 014909 (2014).
- 79. Lagarias, J. C., Reeds, J. A., Wright, M. H. & Wright, P. E. *Convergence Properties of the Nelder–Mead Simplex Method in Low Dimensions*. SIAM J. on Optim. **9**, 112–147 (1998).
- 80. D’Errico, J. *Adaptive Robust Numerical Differentiation*. MATLAB Central File Exchange. 2023.
- 81. Röhrscheid, D. M. & Wolschin, G. *Centrality dependence of charged-hadron pseudorapidity distributions in PbPb collisions at energies available at the CERN Large Hadron Collider in the relativistic diffusion model*. Phys. Rev. C **86**, 024902 (2012).



## ***Acknowledgements***

*I would like to express my deepest gratitude to my academic advisor, Professor Georg Wolschin, whose guidance, invaluable insights, and steadfast support have been instrumental throughout the entirety of this research project.*

*I would also like to thank Professor Andreas Mielke, who has agreed to dedicate some of his time to correcting this thesis.*

*My heartfelt appreciation goes to my family for their unwavering support, encouragement, and understanding throughout this academic journey. Their belief in my abilities and constant encouragement have been a source of motivation.*

*I am grateful to Davide, Luca, and Matteo for sharing this journey with me since it had yet to begin, and for proofreading this thesis. Thanks to Richard for the German version of the abstract, to Yeray for being the greatest deskmate in the office, and to Valentin and all the friends who made these two and a half years go by in the blink of an eye.*

Erklärung:

Ich versichere, dass ich diese Arbeit selbstständig verfasst habe und keine anderen als die angegebenen Quellen und Hilfsmittel benutzt habe.

Heidelberg, den 20.12.2023

A handwritten signature in blue ink, appearing to read "Alvin Dizi", written over a dotted line.